

7-1-2022

## NICER X-Ray Observations of Eta Carinae during Its Most Recent Periastron Passage

David Espinoza-Galeas  
*Catholic University of America*

M. F. Corcoran  
*Catholic University of America*

K. Hamaguchi  
*NASA Goddard Space Flight Center*

C. M.P. Russell  
*Catholic University of America*

T. R. Gull  
*NASA Goddard Space Flight Center*

*See next page for additional authors*

Follow this and additional works at: [https://scholarworks.sjsu.edu/faculty\\_rsca](https://scholarworks.sjsu.edu/faculty_rsca)

---

### Recommended Citation

David Espinoza-Galeas, M. F. Corcoran, K. Hamaguchi, C. M.P. Russell, T. R. Gull, A. F.J. Moffat, N. D. Richardson, G. Weigelt, D. John Hillier, Augusto Damineli, Ian R. Stevens, Thomas Madura, K. Gendreau, Z. Arzoumanian, and Felipe Navarete. "NICER X-Ray Observations of Eta Carinae during Its Most Recent Periastron Passage" *Astrophysical Journal* (2022). <https://doi.org/10.3847/1538-4357/ac69ce>

This Article is brought to you for free and open access by SJSU ScholarWorks. It has been accepted for inclusion in Faculty Research, Scholarly, and Creative Activity by an authorized administrator of SJSU ScholarWorks. For more information, please contact [scholarworks@sjsu.edu](mailto:scholarworks@sjsu.edu).

---

**Authors**

David Espinoza-Galeas, M. F. Corcoran, K. Hamaguchi, C. M.P. Russell, T. R. Gull, A. F.J. Moffat, N. D. Richardson, G. Weigelt, D. John Hillier, Augusto Damineli, Ian R. Stevens, Thomas Madura, K. Gendreau, Z. Arzoumanian, and Felipe Navarete



# NICER X-Ray Observations of Eta Carinae during Its Most Recent Periastron Passage

David Espinoza-Galeas<sup>1,2</sup> , M. F. Corcoran<sup>1,3</sup> , K. Hamaguchi<sup>3,4</sup> , C. M. P. Russell<sup>1,5</sup>, T. R. Gull<sup>6,7</sup> , A. F. J. Moffat<sup>8</sup>,  
N. D. Richardson<sup>9</sup> , G. Weigelt<sup>10</sup> , D. John Hillier<sup>11</sup>, Augusto Daminieli<sup>12</sup> , Ian R. Stevens<sup>13</sup> , Thomas Madura<sup>14</sup>,  
K. Gendreau<sup>15</sup> , Z. Arzoumanian<sup>15</sup>, and Felipe Navarete<sup>16</sup>

<sup>1</sup> Institute for Astrophysics and Computational Sciences, The Catholic University of America, 620 Michigan Avenue, N.E. Washington, DC 20064, USA  
[84espinozagaleas@cua.edu](mailto:84espinozagaleas@cua.edu)

<sup>2</sup> Departamento de Astronomía y Astrofísica, Facultad de Ciencias Espaciales, Universidad Nacional Autónoma de Honduras, Bulevar Suyapa, Tegucigalpa, M.D.C., Honduras, Centroamérica

<sup>3</sup> CRESST and X-ray Astrophysics Laboratory, NASA/Goddard Space Flight Center, Greenbelt, MD 20771, USA

<sup>4</sup> Department of Physics, University of Maryland, Baltimore County, 1000 Hilltop Circle, Baltimore, MD 21250, USA

<sup>5</sup> Department of Physics and Astronomy, University of Delaware, Newark, DE 19716, USA

<sup>6</sup> Exoplanets & Stellar Astrophysics Laboratory, NASA/Goddard Space Flight Center, Greenbelt, MD 20771, USA

<sup>7</sup> Space Telescope Science Institute, 3700 San Martin Drive, Baltimore, MD 21218, USA

<sup>8</sup> Département de physique and Centre de Recherche en Astrophysique du Québec (CRAQ), Université de Montréal, C.P. 6128, Succ. Centre-Ville, Montréal, Québec, H3C 3J7, Canada

<sup>9</sup> Embry Department of Physics and Astronomy, Embry-Riddle Aeronautical University, 3700 Willow Creek Road, Prescott, AZ 86301, USA

<sup>10</sup> Max-Planck-Institut für Radioastronomie, Auf dem Hügel 69, D-53121 Bonn, Germany

<sup>11</sup> Department of Physics and Astronomy & Pittsburgh Particle Physics, Astrophysics and Cosmology Center (PITT PACC), University of Pittsburgh, 3941 O'Hara Street, Pittsburgh, PA 15260, USA

<sup>12</sup> Universidade de São Paulo, IAG, Rua do Matão 1226, Cidade Universitária São Paulo-SP, 05508-090, Brasil

<sup>13</sup> School of Physics & Astronomy, University of Birmingham, Birmingham, B15 2TT, UK

<sup>14</sup> Department of Physics & Astronomy, San Jose State University, One Washington Square, San Jose, CA 95192, USA

<sup>15</sup> X-ray Astrophysics Laboratory, NASA/Goddard Space Flight Center, Greenbelt, MD 20771, USA

<sup>16</sup> SOAR Telescope/NSF's NOIRLab Avda Juan Cisternas 1500, 1700000, La Serena, Chile

Received 2022 January 13; revised 2022 April 1; accepted 2022 April 20; published 2022 July 8

## Abstract

We report high-precision X-ray monitoring observations in the 0.4–10 keV band of the luminous, long-period colliding wind binary Eta Carinae, up to and through its most recent X-ray minimum/periastron passage in 2020 February. Eta Carinae reached its observed maximum X-ray flux on 2020 January 7, at a flux level of  $3.30 \times 10^{-10}$  ergs s<sup>-1</sup> cm<sup>-2</sup>, followed by a rapid plunge to its observed minimum flux,  $0.03 \times 10^{-10}$  ergs s<sup>-1</sup> cm<sup>-2</sup>, near 2020 February 17. The NICER observations show an X-ray recovery from the minimum of only  $\sim 16$  days, the shortest X-ray minimum observed so far. We provide new constraints for the “deep” and “shallow” minimum intervals. Variations in the characteristic X-ray temperatures of the hottest observed X-ray emission indicate that the apex of the wind–wind “bow shock” enters the companion’s wind acceleration zone about 81 days before the start of the X-ray minimum. There is a steplike increase in column density just before the X-ray minimum, probably associated with the presence of dense clumps near the shock apex. During the recovery and after, the column density shows a smooth decline, which agrees with previous  $N_H$  measurements made by Swift at the same orbital phase, indicating that the changes in the mass-loss rate are only a few percent over the two cycles. Finally, we use the variations in the X-ray flux of the outer ejecta seen by NICER to derive a kinetic X-ray luminosity of the ejecta of  $\sim 10^{41}$  ergs s<sup>-1</sup> near the time of the “Great Eruption.”

*Unified Astronomy Thesaurus concepts:* [Stellar winds \(1636\)](#); [X-ray sources \(1822\)](#); [Stellar evolution \(1599\)](#)

*Supporting material:* machine-readable tables

## 1. Introduction

At a distance of  $\sim 2.3$  kpc (Smith 2006), Eta Carinae ( $\eta$  Car; Davidson 1971; Davidson & Humphreys 1997; Humphreys & Martin 2012) is the nearest star system with a mass  $\gtrsim 100 M_\odot$  (Hillier et al. 2001; Corcoran & Ishibashi 2012; Madura et al. 2012). The  $\eta$  Car system is a high-mass noncompact binary system containing an extremely unstable “Luminous Blue Variable” (LBV),  $\eta$  Car-A. In the mid-nineteenth century, this star experienced (and survived) the most energetic stellar mass ejection event ever observed to date, where a mass of  $\gtrsim 45 M_\odot$  (Morris et al. 2017) was ejected. This material created the bipolar

“Homunculus Nebula” (Gaviola 1950), which today surrounds the star and is expanding outward at a velocity of  $650 \text{ km s}^{-1}$  (Davidson & Humphreys 1997). Observations of the He I  $1.083 \mu\text{m}$  emission line over a period of 50 yr reported by Daminieli (1996) established, for the first time, a strict periodicity associated with the stellar spectrum, suggesting that the star is a massive binary system with an orbital period of 5.52 yr (Daminieli et al. 1997). The discovery of periodic X-ray variability (Corcoran et al. 1995; Ishibashi et al. 1999; Corcoran 2005) was critical to identifying the system as a highly eccentric ( $e \approx 0.9$ ) “colliding wind” binary (Corcoran et al. 1998). The X-ray emission observed from the  $\eta$  Car system is dominated by hot shocked gas produced when the dense, slow ( $V_\infty \approx 420 \text{ km s}^{-1}$ ; Groh et al. 2012) wind of the LBV primary  $\eta$  Car-A collides with the wind of its companion star,  $\eta$  Car-B. Because the companion star has never been directly detected, X-ray observations remain critical to constraining its stellar wind

**Table 1**  
 $\eta$  Car Adopted Parameters

Parameter	Value	Reference
Distance (pc)	$2300 \pm 200$	Smith (2006)
Period (X-ray, days)	$2023.40 \pm 0.71$ days	Corcoran et al. (2017)
Eccentricity	0.9	Corcoran et al. (2001)
$T_o$ (Periastron Passage, MJD)	56873.90	Teodoro et al. (2016)
$T_x$ (Deep X-Ray Minimum Start, MJD)	50799.42	Corcoran et al. (2017)
Total Luminosity ( $10^6 L_\odot$ )	5	Hillier et al. (2001)
Mass, $\eta_A$ ( $M_\odot$ )	>100	Hillier et al. (2001)
Mass, $\eta_B$ , ZAMS ( $M_\odot$ )	40–50	Mehner et al. (2010)
$V_{\infty,A}$ ( $\text{km s}^{-1}$ )	420	Groh et al. (2012)
$V_{\infty,B}$ ( $\text{km s}^{-1}$ )	3000	Pittard & Corcoran (2002)
$\dot{M}_A$ ( $10^{-5} M_\odot \text{ yr}^{-1}$ )	$\approx 85$	Madura et al. (2013)
$\dot{M}_B$ ( $10^{-5} M_\odot \text{ yr}^{-1}$ )	$\approx 1.4$	Parkin et al. (2009)
$a$ (AU)	15.9	

properties and monitoring changes in the mass-loss rates from either star. The temperatures inferred from the X-ray spectrum and the X-ray brightness of the gas shocked in the wind collision suggest that the unseen companion star has a fast ( $V_\infty \approx 3000 \text{ km s}^{-1}$ ; Pittard & Corcoran 2002) lower-density wind, probably some type of hot massive star (Verner et al. 2005; Mehner et al. 2010). Table 1 summarizes the stellar and orbital parameters of the  $\eta$  Car system.

X-ray spectra provide important observational constraints on the temperatures and densities in the hot shocked gas in the wind–wind collision “bow shock,” while the absorption suffered by the X-ray emission provides information about the density distribution of the wind of the LBV primary (since the matter along the line of sight to the X-ray source is dominated by the wind of the LBV). These quantities change with the distance between the stars (Stevens et al. 1992), as the stars revolve in their extremely eccentric orbit.

Figure 1 shows previous observations (Ishibashi et al. 1999; Corcoran et al. 2001; Pittard & Corcoran 2002; Corcoran 2005; Corcoran et al. 2010, 2017) of the time-variable X-ray emission from the  $\eta$  Car system. These observations have helped to establish the temperatures and densities of the shocked gas in the wind–wind collision region, and analyses of these observations using even more sophisticated models (Okazaki et al. 2008; Parkin et al. 2011; Madura et al. 2013) have determined the geometry of the shocked winds, the temperatures at the colliding wind region (CWR), and the mass-loss rate of the winds from the stars. Even though published 3D models of the X-ray spectral variability provide a good overall description of the CWR (Parkin et al. 2011; Russell et al. 2016), they do not explain some important details of  $\eta$  Car’s X-ray behavior, such as the “flaring” episodes seen prior to the start of the X-ray minimum (Ishibashi et al. 1999; Moffat & Corcoran 2009), the variation in the recovery from the X-ray minimum (Corcoran et al. 2010), or the “deep”/“shallow” minimum transition (Hamaguchi et al. 2014).

In this paper, we report the first monitoring of the variable X-ray spectrum of  $\eta$  Car with the Neutron Star Interior Composition Explorer (NICER). Here, we discuss the observed X-ray spectrum variations from our NICER X-ray observing

campaign, and compare them to the X-ray variations seen during previous orbital cycles. Throughout the paper, phases are calculated using the X-ray ephemeris (Corcoran et al. 2017), where  $E$  is the cycle count:

$$\text{MJD (X-ray Minimum)} = 50799.4 + 2023.4E. \quad (1)$$

The X-ray epoch  $\phi = 0$  in Figure 1 refers to the first RXTE deep minimum. Previous works, such as Damineli et al. (2008) and Teodoro et al. (2016), have used spectral variations of He emission to number the cycles of  $\eta$  Car, starting from the event observed in 1948 by Gaviola (1953). The square brackets in Figure 1 show the corresponding cycle number based on the He minima. The epoch of the periastron, using the He cycles in the figure, is based on variations of the transient He II  $\lambda 4686$  line,  $T_o = 56873.9$ , found by Teodoro et al. (2016). This He II epoch corresponds to the starting point of cycle 10, which is 4.3 days later than the X-ray minimum for the 1997 periastron passage.

This paper is organized as follows. We describe the NICER observing program and the reduction and analysis of the NICER spectra in Section 2, including a discussion of the NICER background estimation. We present the results of the analysis of the net X-ray spectra in Section 4. We discuss the main results of our spectral analysis in Section 5, including a comparison of the NICER spectral properties with similar properties from previous cycles—and, in particular, we compare the flux variations to refine the X-ray period, and examine the variations prior to and after the start of the X-ray minimum. We summarize our results in Section 6 and discuss areas of future work.

## 2. Observations

### 2.1. Description of the Instrument

NICER (Gendreau et al. 2012; Arzoumanian et al. 2014) is an X-ray astronomy facility attached to the International Space Station (ISS). NICER is devoted to time-resolved X-ray spectrometry in the 0.2–12.0 keV energy band. NICER was launched on 2017 June 3, aboard a Space X Falcon 9 rocket, and deployed at the ISS on 2017 June 16. NICER’s X-Ray Timing Instrument (XTI; Prigozhin et al. 2016) is comprised of a coaligned array of 52 Focal Plane Modules, each consisting of a matched pair of X-ray “concentrator” (XRC) optics with a silicon drift detector (SDD) to record the energy and time of arrival of source X-ray photons. Each XRC optic collects X-rays over a roughly 30 arcmin<sup>2</sup> region of the sky, centered on the target of interest in the 0.2–12 keV energy band, and concentrates them onto an SDD. NICER’s primary mission is to obtain X-ray spectrometry with high time and moderate spectral resolution of cosmic X-ray sources, primarily of X-ray binary pulsars. NICER’s combination of a large effective area, a restricted field of view, and a broad bandpass in the thermal X-ray range makes it especially well suited to observing X-ray variables like long-period colliding wind binaries (and other sources), in addition to X-ray pulsars. Table 2 lists the key technical specifications of NICER’s capabilities.

NICER observed  $\eta$  Car starting on 2017 July 20 (as part of NICER’s “observatory science” program), continuing with guest investigator programs in Cycle 1 (Principle Investigator, M. F. Corcoran) and Cycle 2 (Principal Investigator, D. Espinoza-Galeas). The whole set of NICER observations are listed in the Appendix, but we present a summary of the observations in Table 3. NICER has provided frequent measurements of  $\eta$  Car’s X-ray spectrum, typically twice per

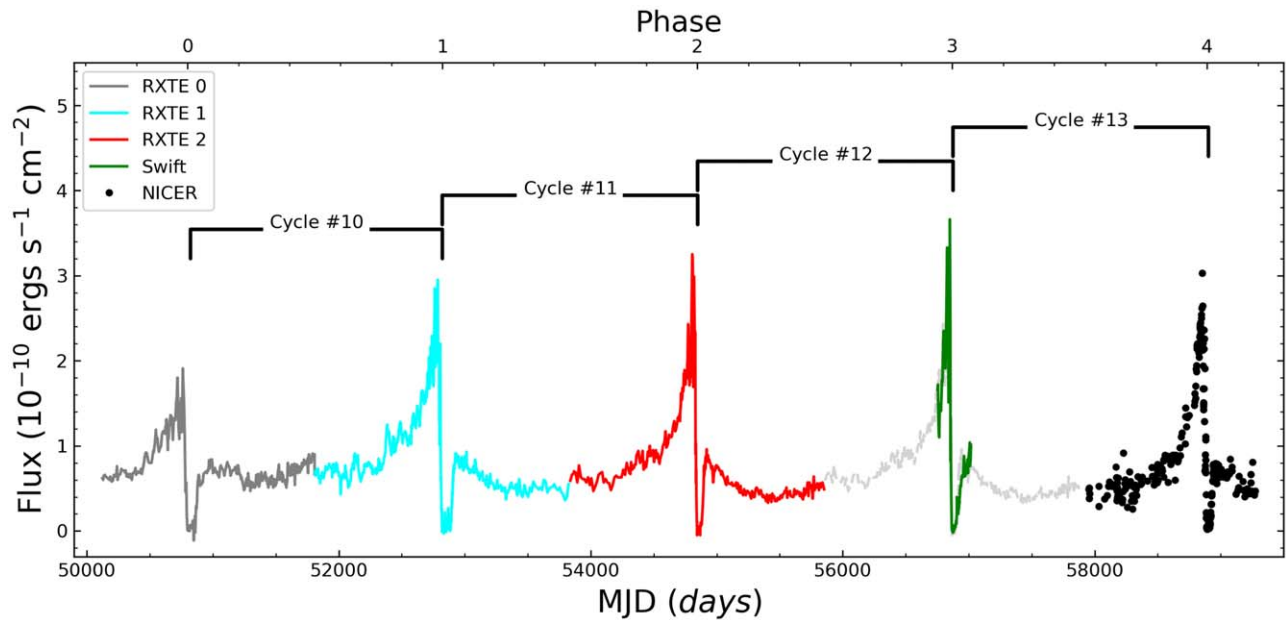


**Figure 1.**  $\eta$  Car’s X-ray lightcurve between 2.0 and 10.0 keV for RXTE and Swift. For easy identification, the observations are color coded and separated in different sets around the X-ray minima. We define  $\phi = 0$  at the X-ray minimum of the first RXTE cycle of observations, using the epoch and period calculated in Corcoran et al. (2017). Corcoran et al. (2017) used the full set of data to find an X-ray periodicity of  $2023.40 \pm 0.71$  days, which is very close to the periodicity of 2022.7 days found by Teodoro et al. (2016) for  $\eta$  Car. The brackets show the corresponding cycle numbers using the He I and II minima events in Damineli et al. (2008) and Teodoro et al. (2016). The light gray dashed line is a repetition of the last RXTE cycle. The plot shows us the variability of the emission in five continuous cycles from 1996 to 2021, including the NICER observations, in black.

**Table 2**  
NICER XTI Characteristics

Property	
Effective area	$>2000 \text{ cm}^2$ at 1.5 keV $600 \text{ cm}^2$ at 6 keV
Energy resolution	85 eV at 1 keV 137 eV at 6 keV
Broad bandpass	$0.2 < E < 12.0 \text{ keV}$
Absolute timing precision	$< 300 \text{ ns}$
Restricted field of view	$30 \text{ arcmin}^2$
Sensitivity	$3 \times 10^{-14} \text{ ergs s}^{-1} \text{ cm}^{-2}$ (0.5–10.0 keV, $5\sigma$ in 10 ksec)

**Table 3**  
 $\eta$  Car Observation Summary

	# of Obs.	First Obs.	Last Obs.
CHANDRA	31	2000-11-19	2020-1-26
NICER	249	2017-7-21	2021-2-21

month, with appropriately increased sampling near the periastron, when the variation in the X-ray spectrum occurs on timescales of days. An alternative analysis of some of these spectra has been provided by Kashi et al. (2021).

## 2.2. Data Reduction and Calibration

The NICER spectra for all  $\eta$  Car observations were extracted from the clean, merged photon events file, using data obtained outside of the South Atlantic Anomaly at Sun angles  $>40^\circ$ , to avoid optical stray light contamination, using the NICERDAS<sup>17</sup>

<sup>17</sup> <https://heasarc.gsfc.nasa.gov/docs/software/lheasoft/help/nicer.html>

software package distributed with the HEASoft software analysis package (version 6.27.2). We used the standard NICER event cleaning criteria<sup>18</sup> to convert the observed event times and pulse heights to cleaned events with calibrated energies, using data from all 52 active detectors. We used calibration data (effective areas and instrument response functions) from the publicly available NICER calibration data, version 20200202.

## 2.3. NICER Background Estimation

NICER is subject to a varying charged particle environment in the high-inclination ISS orbit, which traverses regions of trapped charged particles near the South Atlantic Anomaly and the regions near the north and south poles (the “polar horns”). The charged particle background is most noticeable at high energies. At low energies, the NICER background is dominated by optical light contamination at low Sun angles and an instrumental “noise peak” of excess events at energies  $<0.4 \text{ keV}$ . Correction for background is important, especially near the X-ray minimum. To minimize the background contamination in the NICER spectra, we extracted lightcurves in the 0.4–10 keV band for all the NICER observations and visually inspected them, defining time regions to exclude short intervals of large rapid increases in count rate produced by the variable charged particle environment. We then extracted X-ray spectra for each observation from the cleaned and screened event files. Residual charged particle background and/or optical light contamination generally affects spectra even after the exclusion of obvious intervals of high background.

Background estimation is still under development, so we used two different background estimator tools provided by the

<sup>18</sup> See <https://heasarc.gsfc.nasa.gov/lheasoft/ftools/headas/nimaketime.html> for a description of the standard cleaning criteria.

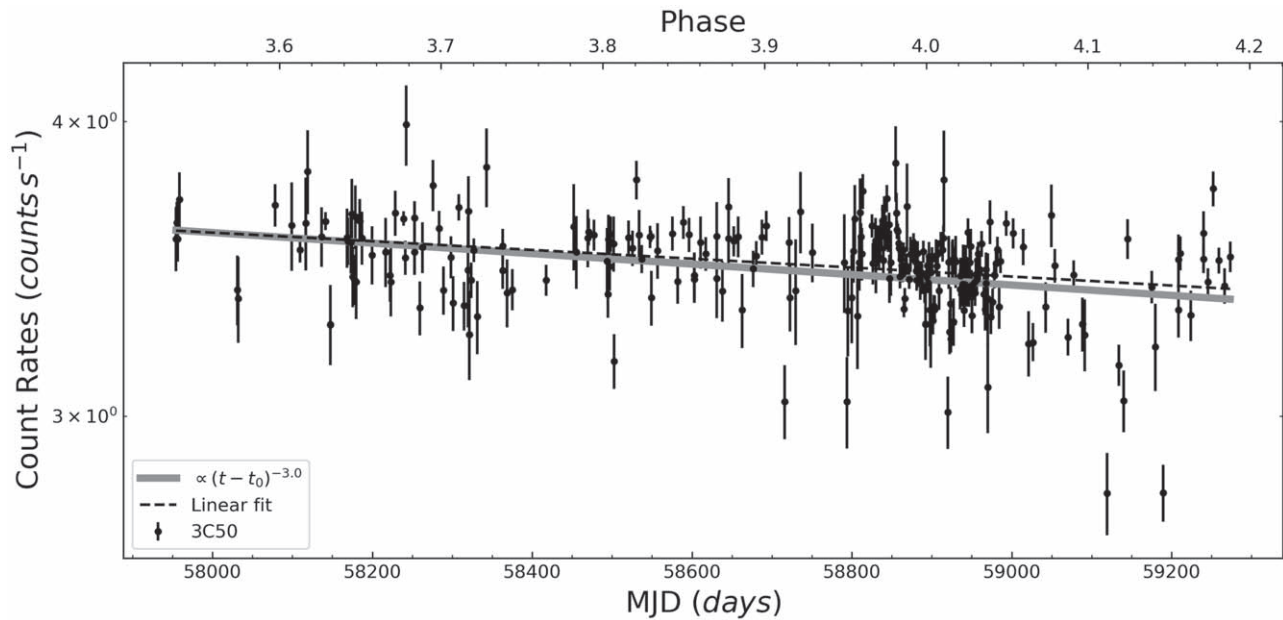


**Figure 2.** Count rates for  $\eta$  Car between 0.5–1.0 keV observed by NICER after background correction using the `nibackgen3C50` model. The emission in this soft band is produced by the shocked gas in the extended outer debris region around  $\eta$  Car, and is expected to be constant over timescales of months–years. The slight decline of  $\eta$  Car’s soft X-ray emission (dashed black line) shows good agreement with the  $\propto(t - t_0)^{-3}$  power law (gray line), assuming that the ejecta originated near the time of the Great Eruption in 1843 (Kiminki et al. 2016).

NICER Guest Observer Facility,<sup>19</sup> the `nibackgen3C50` (Remillard et al. 2021) and the `nicer_bkg_estimator` “space weather” (SW) background estimators. Both estimators use NICER observations of “blank-sky” fields (i.e., fields with no obvious sources in the XRC field of view) to estimate the background. The `nibackgen3C50` tool compares NICER spectra in various bands in the observed and blank-field observations to construct a background, while the `nicer_bkg_estimator` tool matches the Sun angle, cutoff rigidity, and solar Kp index between the observation and NICER observations of “blank-sky” regions to estimate the amount of background due to optical loading and the charged particle environment. Because background estimates continue to be refined, we used both models to gauge the effects of background contamination, but because the SW background estimator showed more dispersion in the  $\chi^2_{\text{red}}$  value of the fittings, we adopted the `nibackgen3C50` backgrounds in our analysis.

As a check on the background estimation, Figure 2 shows the total count rates for  $\eta$  Car between 0.5 and 1.0 keV, along with the net rates using the backgrounds estimated from the `nibackgen3C50` method. In this range, the X-ray emission is totally dominated by the emission from the “Outer Ejecta” (OE) region surrounding the Homunculus Nebula (Seward et al. 1979; Weis et al. 2004; Hamaguchi et al. 2007a). The emission from the OE region, which extends out to  $\sim 1'$  from  $\eta$  Car, is entirely within the  $1.7$  radius of the field of view of the NICER SDDs, and so present in all NICER observations of  $\eta$  Car. The mean of the total source + background rates in the 0.5–1.0 keV band is  $\mu_{\text{total}} = 3.76 \pm 0.15$  cts  $s^{-1}$ , while the mean of the net count rate using the `nibackgen3C50` method is  $\mu_{\text{net,3c50}} = 3.48 \pm 0.14$  cts  $s^{-1}$ , and the mean of the net count rate using the SW `nicer_bkg_estimator` method is  $\mu_{\text{net,SW}} = 3.55 \pm 0.20$  cts  $s^{-1}$ . In this band, the

`3c50` method appears to have a slightly smaller standard deviation, but is similar to that for the total band. Figure 2 shows the net NICER count rates in the 0.5–1.0 keV band using the `nibackgen3C50` background estimate. The net NICER count rates in this band seem to show a decline of about 7% over the  $\sim 1000$  days of the NICER monitoring, which is also visible in the gross rates and the net rates corrected using the SW model. A linear fit to the total (non-background-subtracted) count-rate data yields a decline of  $\Delta R / \Delta t = 0.150 \pm 0.028$  cts  $ks^{-1} \text{ day}^{-1}$ . We suspected that this apparent decline was instrumental, as might be expected from increasing condensation on the focal plane modules, but the examination of the NICER observations of the supernova remnant 1E 0102.2–7219, an extended soft source, covering the same time span as the  $\eta$  Car observations, did not find a comparable decline in the soft-band flux. This decrease might then be due to the expansion of the OE.  $\eta$  Car’s X-ray emission below 2.0 keV comes from gas heated by the shocked ejecta from the nineteenth-century eruption. The X-ray flux is proportional to the emission measure  $F_X \propto n^2 V$ , where  $n$  is the particle density and  $V$  is the emission volume of hot gas. Assuming a constant mass  $M$  of gas expanding freely at a constant velocity  $v$ , then  $F_X \propto (t - t_0)^{-3}$ . Figure 2 shows how the  $(t - t_0)^{-3}$  power law gives good agreement with the observed  $\eta$  Car soft X-ray emission, assuming that the gas expansion started near the time of the Great Eruption in 1843. The  $(t - t_0)^{-3}$  decline in X-ray flux is observed in the soft X-ray emission (0.3–2.0 keV) of young supernova remnants (Immler & Kuntz 2005). Extrapolating this power law to 100 days after the Great Eruption, the initial X-ray luminosity of the shocked ejecta would have been  $L_{x,0} \sim 3 \times 10^{41}$  ergs  $s^{-1}$ . This would be close to the total luminosity at longer wavelengths derived from the observed brightness of the system at that time ( $L = 10^{(7.3)} \sim L_{\odot}$ ; Davidson & Humphreys 1997). If confirmed, this would be the first estimate of the X-ray luminosity of the Great Eruption.

<sup>19</sup> [https://heasarc.gsfc.nasa.gov/docs/nicer/tools/nicer\\_bkg\\_est\\_tools.html](https://heasarc.gsfc.nasa.gov/docs/nicer/tools/nicer_bkg_est_tools.html)

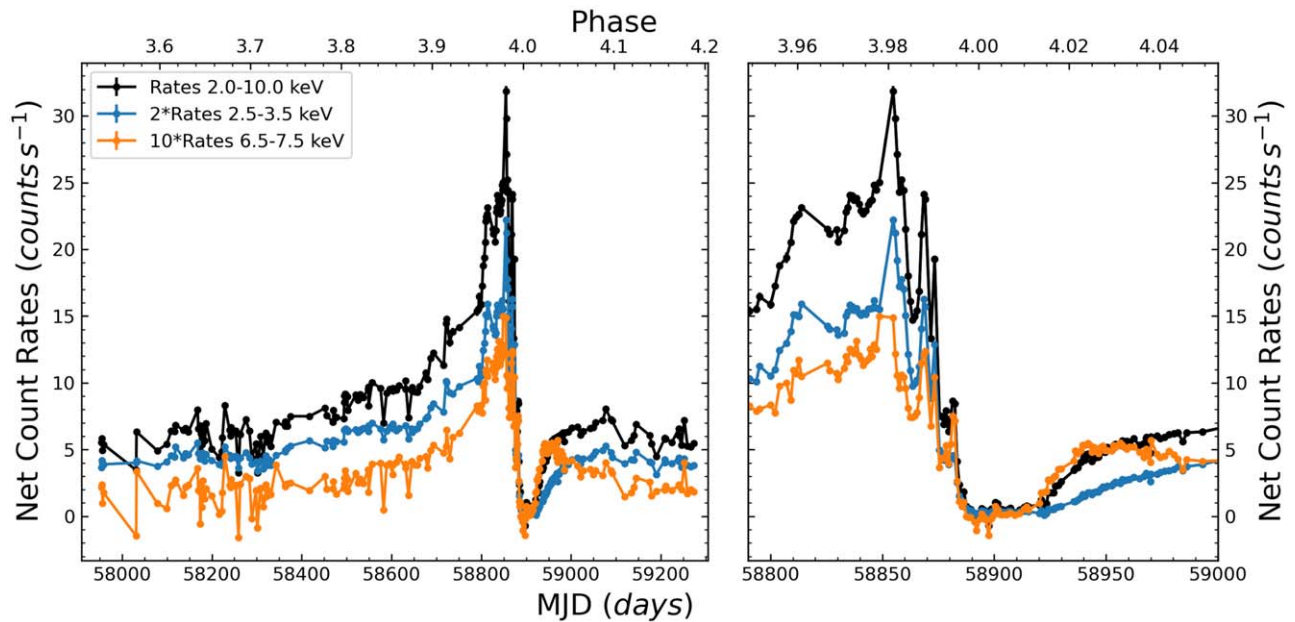


**Figure 3.** NICER net count rates for  $\eta$  Car using the “3c50” background model, in three energy bands. The 2.5–3.5 and 6.5–7.5 keV count rates have been multiplied by  $2\times$  and  $10\times$ , respectively, for display purposes.

### 3. Multiband X-Ray Variations

#### 3.1. NICER Broadband X-Ray Lightcurves of $\eta$ Car

Measurements of the net count rates in the 2.5–3.5, 6.5–7.5, and 2.0–10.0 keV bands are shown in Figure 3. The rates in these three bands are dominated by emission from the hot gas in the colliding wind shock, and the background contamination is fairly low. The 2.0–10.0 keV band was originally adopted by Ishibashi et al. (1999) in their analysis of the RXTE monitoring observations of  $\eta$  Car, and includes nearly all of the observable thermal X-ray emission from the CWR, while excluding contamination from the OE region that is of lower energy.

The net count rates soon after the start of the NICER observations (on MJD 57954.5; 2017 July 20) show significant artificial scatter from observation to observation because of variations in background that are not accurately accounted for by the background model. To mitigate this variability, we requested that the observations obtained after MJD 58306 (2018 July 7) be restricted, to avoid times of low geomagnetic rigidity, i.e., when the ISS was not near the South Atlantic Anomaly or the polar horns. This restriction significantly reduced the variability from the charged particle events, which accounts for the reduced scatter after that time.

The X-ray variability seen by NICER in the 2–10 keV band is similar to that seen in other cycles by the RXTE Proportional Counter Array and the Swift X-ray Telescope. As shown in Figure 3, the count rates in all energy bands show a gradual increase from MJD 57954.5 (2017 July 20) to MJD 58610 (2019 May 7). After MJD 58610, the count-rate increase accelerates, and short-term brightenings (“flares”; Moffat & Corcoran 2009) occur as the stars approach the X-ray minimum near the periastron passage. Starting at MJD 58855 (2020 January 6, about  $\phi \sim 0.98$ ), a rapid decline in the X-ray count rate began, reaching to the “deep” X-ray minimum near MJD 58893 (2020 February 14). The emission in this band had started to increase by MJD 58912.5 (2020 March 4), just 19.5 days after the start of the deep minimum.

The 6.5–7.5 keV band is dominated by high-energy thermal emission, and includes emission in the Fe–K region. This band is not greatly affected by the absorption from the wind of the LBV, except at phases very close to the X-ray minimum when column densities in excess of  $10^{23} \text{ cm}^{-2}$  arise. The flares in the 6.5–7.5 keV band are somewhat smaller in amplitude compared to those in the 2–10 keV band, and there is also evidence that the flares begin sooner in the 6.5–7.5 keV band than at lower energies. All the flares are present in the 2.5–3.5 and 6.5–7.5 keV bands, except for the last flare just before the X-ray minimum. The last flare occurs only in the 6.5–7.5 keV band, while the 2.5–3.5 keV band count rates stay almost constant. The plunge to the X-ray minimum in the 6.5–7.5 keV band seems to occur almost simultaneously with the drop seen in the lower-energy bands, and the X-ray minimum flux is reached at MJD 58854 (2020 January 6) in all energy bands. The X-ray count rates in the all bands begin to increase by MJD 58912.5 (2020 May 4), but at different rates. The rate of increase is greatest in the 6.5–7.5 keV band, and the net rates in this band increase until MJD 58942 (2020 April 3), when they begin to start a slow decline, as the stars separate toward apastron. Of the three bands, the rate of increase is slowest in the low-energy 2.5–3.5 keV band, which shows the importance of the extended absorption of the low-energy X-rays by the intervening, unshocked wind of  $\eta$  Car-A. This absorption continues for about 200 days after the periastron passage.

#### 3.2. Hardness Variations

We calculated the hardness ratio  $HR = (H - M)/(H + M)$ , where  $H$ , the hard band, is defined as the net count rates between  $6.5 < E < 7.5$  keV, and the medium energy band,  $M$ , as the net count rates between  $2.5 < E < 3.5$  keV. We chose these bands because both are dominated by the colliding wind source, with (generally) minimal background contamination, and because the medium band is also sensitive to changes in absorption (as shown in Figure 6), more so than the hard band. This hardness ratio (HR) mainly provides a measure of how the

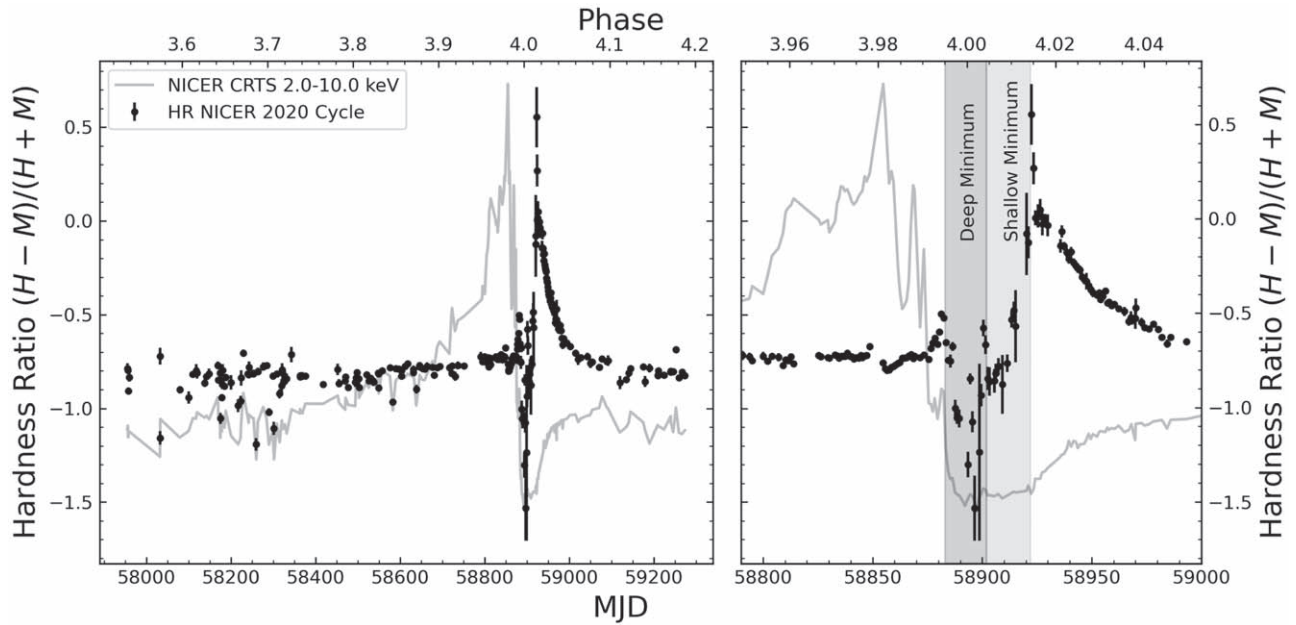


**Figure 4.** HR observed by NICER using a medium band between 2.5–3.5 keV and a high band between 6.5–7.5 keV. The gray regions show the boundaries of the “deep” and “shallow” X-ray minima. The abrupt decline in the HR marks the start of the deep minimum. The abrupt rise in the HR marks the end of the deep minimum and the start of the shallow minimum. The shallow minimum interval ends when the 2–10 keV flux begins to noticeably increase and the observed hardness is at its maximum, indicating the reemergence of highly absorbed emission from the CWR.

absorption to the X-ray source is changing over time, since changes in the shock temperature should be modest, because for most of the orbit the winds collide at terminal velocity.

Figure 4 shows the derived HR from the NICER observations. The HR shows a nearly linear increase, with a small positive slope from midcycle near the apastron to about 20 days before the start of the X-ray minimum, indicating that the hard-band flux increases more rapidly compared to the soft-band flux, probably due to residual absorption in the soft band. After this, there is a significant increase in the HR occurring in a short phase interval,  $\Delta\phi \approx 0.005$  days, due to a combination of the increase in the emission measure of the shocked wind from the secondary and the increased absorption by the wind of  $\eta$  Car-A, as the colliding wind shock starts to move closer to and behind the primary star. This hardness increase happens at the same time as the colliding wind flux is at its observed maximum, just before the plunge to the minimum. When the plunge to the flux minimum starts, the HR also decreases, implying that the higher-energy emission is decreasing rapidly compared to the lower-energy emission. This abrupt decline marks the start of the “deep” X-ray minimum, when the source spectrum is dominated by soft emission from the “Central Constant Emission” (CCE) component (Hamaguchi et al. 2007b), the cosmic background in the NICER field of view, and the uncertainties on the correction of the background contamination, plus the colliding wind source emission is depressed.

Shortly thereafter, the HR abruptly increases, marking the end of the deep minimum, followed by a short interval during which the HR continues to increase, but at a slower rate. This time corresponds to the “shallow” part of the X-ray minimum. As the colliding wind source strengthens, the HR abruptly reaches a maximum (corresponding to the end of the postminimum flux increase in the 6.5–7.5 keV band shown in Figure 3), then declines in a quasi-exponential fashion, as the

colliding wind emission increases but the soft-band emission is still heavily absorbed by the wind of  $\eta$  Car-A.

#### 4. The NICER X-Ray Spectrum

Figure 5 shows NICER spectra from the last X-ray maximum (2020 January 6), through the plunge, until the last X-ray minimum (2020 February 10). Figure 5 is similar to Figure 2 in Kashi et al. (2021), but chosen to avoid flare peaks. Some strong emission lines are marked. The first three spectra show a gradual decline in count rate above 1.5 keV. By February 5, the harder X-ray emission near 1.5 keV is so low that the CCE is clearly observed in the region close to 2.0 keV. The strong Fe XXV feature is still present on February 5, indicating that the hard X-ray emission disappears completely only at the minimum.

Figure 6 shows a sample of four NICER spectra of  $\eta$  Car from the X-ray minimum (2020 March 1, in blue) to three months later, after the X-ray emission has completely recovered from the X-ray minimum (2020 June 1, in blue). Figure 6 can be compared to Figure 4 from Hamaguchi et al. (2007b), which shows a similar montage of the XMM-Newton spectra of  $\eta$  Car from 2003. The colliding wind emission cannot be seen below 1.5 keV, due to the absorption from the Homunculus Nebula, which corresponds to  $N_H \sim 3 \times 10^{22} \text{ cm}^{-2}$ . The emission below 1.0 keV comes from the OE and does not change significantly. The emission above 4.0 keV recovers faster than the emission between 2.0 and 4.0 keV, since it is less affected by absorption, as can be seen by comparing the March 19 and March 1 spectra. By 2020 April 3 ( $\sim 30$  days after the start of the X-ray minimum) the flux above 4 keV has fully recovered, with the colliding wind flux below 4 keV continuing to increase through June 1. The emission above 1.5 keV is mostly thermal emission from hot shocked wind from the companion star,  $\eta$  Car-B, while below 1.5 keV the emission is dominated by the soft thermal emission in the OE. It is worth noting that the Fe XXV line can be detected by



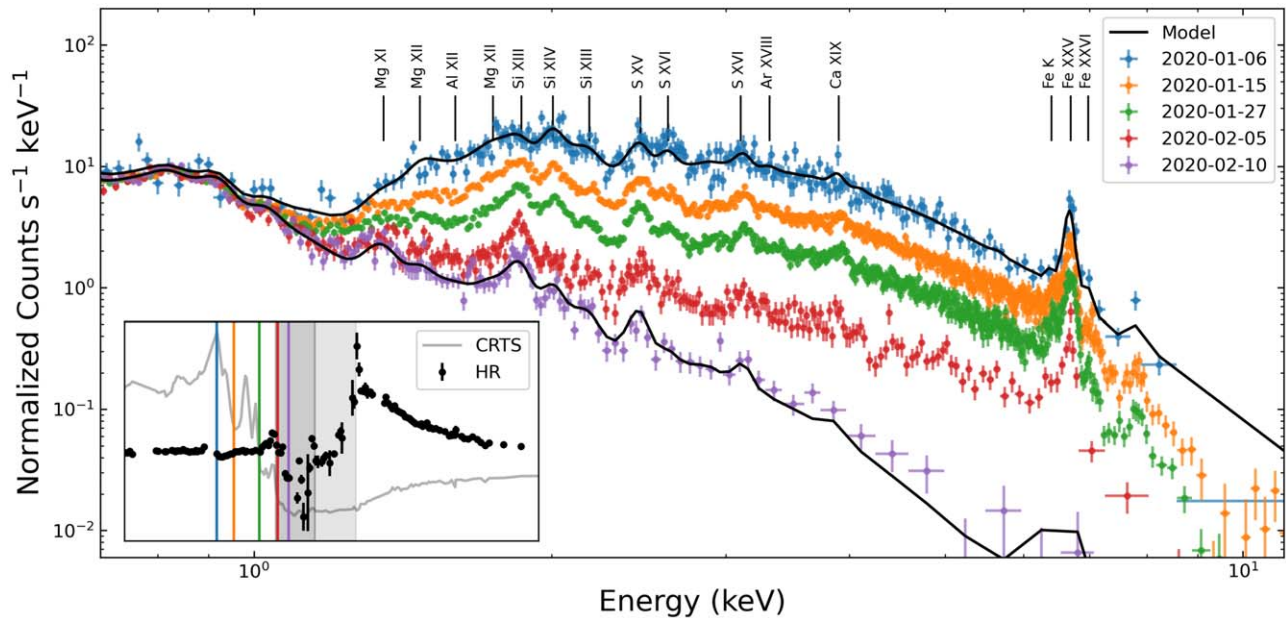


**Figure 5.**  $\eta$  Car spectrum at different phases during the X-ray plunge. The plot has different spectra before the last X-ray minimum, showing the decrease of the spectrum. The inset shows the HR in black and the count rates in gray against time. The color-coded lines show the times when the spectra were observed and the gray regions are the deep and shallow minima, respectively. We can see the changes above 1.0 keV. The three upper spectra show evenly distributed declines in count rates at energies  $>1.0$  keV. By the moment of the fourth observation, in red, we start to notice a decline in the midrange energies between 1.5–4.0 keV. The last spectrum is seven days before the X-ray minimum—notice the disappearance of the high-energy band above 4.0 keV.

NICER even in a short (889 s) observation during the X-ray minimum. In addition to the thermal line emission, NICER clearly shows the Fe–K fluorescence line at 6.4 keV (see Corcoran et al. 1998) blended with the 6.7 keV Fe XXV triplet.

#### 4.1. X-Ray Template Model

$\eta$  Car’s spectra vary over different phases, changing the physical parameters that produce the X-ray emission from the CWR. In order to obtain a better estimation of the temperatures and the column densities from the NICER spectra, we used an  $\eta$  Car spectrum template with all the available dispersed spectra from CHANDRA HETG (Espinoza-Galeas & Corcoran 2020; Espinoza-Galeas 2021, D. Espinoza-Galeas et al. 2022, in preparation). We combined the 32 CHANDRA HETG observations in Table 4 to obtain a high-precision dispersed X-ray spectrum, with a total exposure of 2 Msec and an exposure-weighted average phase of 0.73. This is the highest-precision, highest-spectral resolution spectrum of  $\eta$  Car currently available. We fit the combined spectrum with a linear combination of a small number of collisionally ionized plasma models,<sup>20</sup> plus a Gaussian line to model the fluorescence Fe–K emission line, plus absorption (Wilms et al. 2000). The NICER spectra are not sensitive to the broadening of emission lines, but using the CHANDRA combined spectrum it was clear that a velocity-broadened model was necessary. We found that two velocity-broadened nonsolar abundance thermal components were sufficient to describe the combined HETG spectrum. We used the CHANDRA combined spectrum as a template model to fit each NICER spectrum to derive the X-ray spectral parameters. We fixed the abundances and line broadening to the CHANDRA values when fitting the NICER spectra.

To model the NICER spectra, we also added to the HETG model a third nonvariable thermal component, to account for the nonvariable soft emission below 1.5 keV from the shocked gas in the OE (which is not strongly visible in the HETG spectrum). The initial spectral model parameters are given in Table 5. We then fit all the net NICER spectra, allowing the temperatures, column densities, and emission measures (normalization) of the two colliding wind components to vary, with other components and the OE emission component held fixed.

A complete, detailed analysis of the combined HETG CHANDRA spectrum is available in Espinoza-Galeas (2021). To compare NICER temperatures and column densities, we also present preliminary results of the temperatures and column densities using the individual HETG CHANDRA spectra (D. Espinoza-Galeas et al. 2022, in preparation).

#### 4.2. Flux Variations

Figure 7 shows the NICER flux between 2.0 and 10.0 keV for all the NICER observations, using the `nibackgen3C50` estimator to correct for background, although this model overestimates the background for a small number of observations under conditions of high background. The bottom panel shows the reduced  $\chi^2$  value for all the fits, which are generally acceptable, except close to the X-ray minimum, when the uncertainties on the background subtraction play a significant role in defining the net spectrum. The inset highlights the variations near the X-ray minimum.

Figure 8 shows the flux between 2.0 and 10.0 keV in  $10^{-10}$  ergs  $s^{-1}$   $cm^{-2}$  compared with the RXTE and Swift fluxes in the same band (taken from Corcoran et al. 2017). The three telescopes have instrumental differences and different fields of view, which can cause differences in the flux in the same range, due to the varying amounts of cosmic and instrumental background contamination and other factors. We calibrated the data from NICER with the RXTE and Swift data by

<sup>20</sup> <http://atomdb.org/>

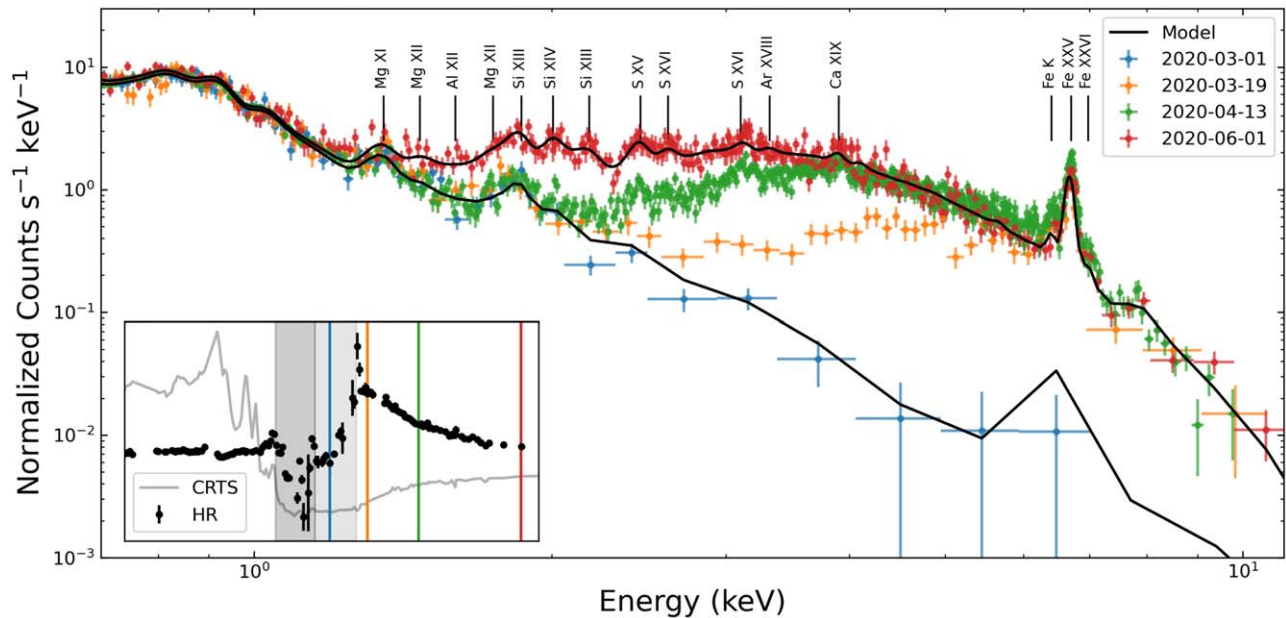


**Figure 6.**  $\eta$  Car spectrum at different phases after the X-ray minimum. The plot has different spectra after the last X-ray minimum, showing the recovery of the spectrum. As in Figure 5, we can follow the changes above 1.0 keV during the recovery, and the inset with the same color coding as the spectra shows the HR and the count rates against time. The blue spectrum is in the shallow minimum, and does not show emission above 4.0 keV. By the time that  $\eta$  Car’s X-ray emission is out of the shallow minimum, the high X-ray emission above 4.0 keV has recovered, but the midrange energies are highly affected by column density (see Figure 11), which here is reflected in the HR on the inset plot. In the last two spectra (green and red), we can see how the midrange X-ray emission continues to recover slowly, after months of the X-ray minimum, while the emission  $>4.0$  keV has completely recovered after the exit from the shallow minimum.

subtracting a small amount of flux from each flux measure, to match the flux of the X-ray deep minimum in all the cycles. During the deep minimum, the net flux is close to the cosmic X-ray background, and the flux differences are minimal then.

The X-ray flux from a colliding wind shock in an eccentric binary should vary inversely with the separation  $D$  of the stars (Stevens et al. 1992; Usov 1992) if the shock cools adiabatically. The smooth dashed curve in Figure 8 shows a  $1/D$  variation using the orbital elements in Table 1. For most of the orbit, the NICER 2–10 keV X-ray flux agrees with the  $1/D$  curve, but starts to deviate from it 10 days before the X-ray minimum is reached. Prior to the X-ray minimum, the RXTE fluxes lie on the  $1/D$  curve that fits the NICER data, though the agreement is better about 80 days after the X-ray minimum.

Once reaching the maximum flux, the NICER lightcurve shows the same plunge into the X-ray minimum as seen in the earlier orbital cycles, as shown in the inset in the upper panel of Figure 8. The X-ray minimum is caused by a combination of an eclipse and the disruption of the shock around  $\eta$  Car-B by the wind of  $\eta$  Car-A, as discussed by Hamaguchi et al. (2014). According to Equation (1), the deep X-ray minimum should have been reached around 2020 February 14. NICER observed the deep minimum around 2020 February 13, as we reported in Corcoran et al. (2020).

Based on the behavior shown in previous cycles, the end of the X-ray minimum was expected no earlier than the end of March. But the NICER data show a clear increase in flux between 0.5 and 9.0 keV, starting approximately on 2020 March 15 (MJD 58923.0; Espinoza-Galeas et al. 2020). This is the earliest recovery of  $\eta$  Car’s X-ray emission yet observed. The flux increase from the minimum in the 2–10 keV band ended by MJD 58950 (2020 April 11). The analogous analysis in Kashi et al. (2021) shows similar results, confirming our announcement in Espinoza-Galeas et al. (2020).

#### 4.3. The X-Ray Period

We redetermined the X-ray period, including the NICER data, using a simple implementation of a phase dispersion minimization technique (Stellingwerf 1978). We phase-folded the four X-ray flux curves from RXTE, Swift (Corcoran et al. 2017), and NICER using trial periods in the range of 2015–2035 days. For each trial period, we interpolated each flux curve to a common phase scale, assuming a common epoch, then calculated the sum of the residuals between the three flux curves relative to the NICER fluxes. Figure 9 plots the summed residuals versus test phase. We found that a period of  $2023.03 \pm 1.12$  days yielded the smallest summed residuals. This period is 0.36 days shorter than the X-ray period derived by Corcoran et al. (2017), and 0.33 days longer than the period derived from analysis of the He II  $\lambda 4686$  emission line by Teodoro et al. (2016).

Corcoran et al. (2017) calculated an error of 0.71, which is smaller than our calculation. This is probably due to the high variability of the first observations made with high-background conditions. But the calculation of the period in this work is still in very good agreement with Teodoro et al. (2016) and Corcoran et al. (2017). We decided to keep the period of  $2023.40 \pm 0.71$  days to try to avoid the uncertainty added by the first NICER observations.

#### 4.4. X-Ray Flaring

Just prior to the minimum, the X-ray emission from  $\eta$  Car brightens and undergoes a period of rapid variability (“flares”), which have been observed by RXTE, Swift, and now NICER. The X-ray “flaring” seen by NICER was first observed on MJD 58802 (2019 November 15; Corcoran et al. 2019), about 90 days prior to the X-ray minimum, similar to the start of the flare interval seen by RXTE and Swift. During the flare interval, the X-ray flux in the 2–10 keV band changes dramatically on

**Table 4**  
HETG CHANDRA Observations

Obsid	Expt	Date	MJD	Phase
632	89545.68	2000-11-19T02:47:43	51867.65	0.527
3749	91280.92	2002-10-16T08:09:53	52563.89	0.871
3745	94533.00	2003-5-2T11:57:20	52762.07	0.969
3748	97249.20	2003-6-16T05:36:31	52806.82	0.991
7445	25393.24	2008-10-15T20:18:41	54755.01	1.954
10787	68904.23	2008-10-21T23:11:26	54761.38	1.957
10831	17589.25	2008-12-8T12:31:41	54808.63	1.980
8930	29646.37	2008-12-10T01:49:02	54810.26	1.981
10827	27365.77	2008-12-12T17:34:07	54812.90	1.983
10895	15257.55	2009-3-16T17:18:12	54906.82	2.029
10894	21986.45	2009-3-17T21:26:40	54908.04	2.030
9945	31275.61	2009-4-21T06:46:35	54942.48	2.047
10905	26298.47	2009-4-26T13:56:49	54947.75	2.049
9946	56628.15	2009-9-6T20:45:21	55081.21	2.116
11992	18428.78	2009-12-21T12:52:08	55186.66	2.167
11017	17454.93	2009-12-22T09:47:25	55187.52	2.168
12064	17703.14	2009-12-23T03:48:06	55188.28	2.168
12065	18625.89	2009-12-23T23:44:42	55189.11	2.168
11993	43826.40	2010-11-14T13:33:42	55514.84	2.329
11994	39364.24	2010-11-21T07:26:40	55521.56	2.333
12358	102189.1	2011-10-20T11:19:40	55855.10	2.497
13670	31173.59	2012-10-19T16:25:08	56219.88	2.678
15569	68162.57	2012-10-20T17:29:41	56221.15	2.678
21177	29027.65	2019-5-16T02:58:19	58619.31	3.863
22218	15446.14	2019-5-17T00:32:15	58620.12	3.864
22219	33862.69	2019-5-18T17:35:26	58621.94	3.864
21178	29024.17	2019-7-1T17:56:35	58665.93	3.886
22272	27089.92	2019-7-2T10:13:04	58666.60	3.887
22273	15489.07	2019-7-4T10:01:32	58668.52	3.887
21179	57150.21	2019-8-27T05:54:31	58721.71	3.914
21180	24249.47	2019-10-8T13:56:11	58764.74	3.937
22310	19570.27	2020-1-6T01:58:12	58854.21	3.981
23117	19570.34	2020-1-6T17:13:59	58854.84	3.981
23119	19567.59	2020-1-11T06:06:16	58859.38	3.983
22311	34169.62	2020-1-13T11:07:07	58861.68	3.984
23126	34168.16	2020-1-14T10:03:59	58862.63	3.985
22846	29302.70	2020-1-16T02:34:15	58864.29	3.986
22847	14703.70	2020-1-26T16:22:24	58874.78	3.991
23131	33195.76	2020-1-27T16:42:56	58875.90	3.991

timescales of days. This rapid X-ray variability has been seen by all three instruments. However, the RXTE cycle 0 observations were not obtained as frequently as the observations in the latter cycles, which meant that some of the short-timescale variations were not sampled as completely as they were in subsequent cycles. Except for the undersampled RXTE cycle 0 observations, the maximum fluxes in the flares are similar.

To quantify the flaring observed by NICER, we adopted a process similar to that used by Moffat & Corcoran (2009); namely, we estimate an underlying smooth flux baseline by eye, and then subtract this baseline from the net NICER fluxes. One difference with the Moffat & Corcoran (2009) analysis is that we use observations that closely follow the  $1/D$  line in Figure 8 for the baseline flux. We also use the same NICER baseline flux to calculate the RXTE and Swift residuals. The NICER fluxes, the baseline, and the residuals are shown in Figure 10. In Figure 10, the NICER measures are shown versus time, using the epoch of the periastron  $T_o$  given by Corcoran et al. (2017). Figure 10 also compares the residuals for the RXTE and Swift data (we do not include the first set of RXTE

**Table 5**  
Initial Spectrum Model

Parameter	Cooler Comp	Hotter Comp	Outer Ejecta Comp
NH ( $10^{22}$ cm $^{-2}$ )	3.00	10.00	0.60
kT (keV)	1.26	4.43	0.25
Redshift	0.00	0.00	0.00
Broadening (km s $^{-1}$ )	598.00	888.88	900.00
He	1.00	fixed	fixed
C	1.00	fixed	fixed
N	20.00	fixed	fixed
O	1.00	fixed	fixed
Ne	1.00	fixed	fixed
Mg	0.59	fixed	fixed
Al	0.47	fixed	fixed
Si	0.41	fixed	fixed
S	0.46	fixed	fixed
Ar	0.66	fixed	fixed
Ca	0.88	fixed	fixed
Fe	0.51	fixed	fixed
Ni	1.00	fixed	fixed

**Note.** Elemental abundances are relative to solar values, using Anders & Grevesse (1989). The model also includes a variable Gaussian iron K line near 6.4 keV.

observations, since the sampling frequency was not as high as in the later two cycles).

We note that Moffat & Corcoran (2009) argued that long-duration, low-intensity X-ray flares could be seen near the apastron in the RXTE observations. But the NICER observations near the apastron were obtained at the start of the mission, and were affected by variations in the local charged particle background and scattered solar radiation, so we cannot claim that the variations before MJD = 58308 days ( $\sim\phi = 3.71$ ) are signs of intrinsic source X-ray variability. After  $\phi = 3.71$ ,  $\eta$ Car's NICER observations started to be taken at low-background conditions.

After MJD = 58400 ( $\sim\phi = 3.75$ ), Figure 10 shows a small excess seen by NICER during the rise to the X-ray maximum. Similarly, the excess in the residuals for the RXTE and Swift observations increases after  $\phi = 3.75$ . At phases  $\sim\phi > 3.93$ , the RXTE and Swift residuals show a decrease in the width of the flares. The shortening between the flares can be seen by NICER just until  $\phi = 3.95$ , since we do not have observations between  $3.92 > \phi > 3.95$ . The plot shows a breakup at  $\phi \approx 3.97$ , when the X-ray flux is approaching its maximum. The flares are not clearly seen at the same time in each orbital cycle, though some coincidences between cycles do occur. After the X-ray maximum flux, during the plunge, the flares peaks show more coincidences between different cycles, but this could just be a bias due to the fast orbital motion close to the periastron passage.

#### 4.5. Variations in X-Ray Absorption

Figure 11 shows the derived variation in column density from the analysis of the NICER spectra compared to the column densities derived from the analysis of the Swift spectra in 2014 (Corcoran et al. 2017). The NICER column densities show substantial scatter between  $2 \times 10^{22}$  and  $2 \times 10^{23}$  cm $^{-2}$ , before phase 3.97. The derived column densities may be influenced by the uncertainties on our estimate of the background and contamination from the soft OE emission

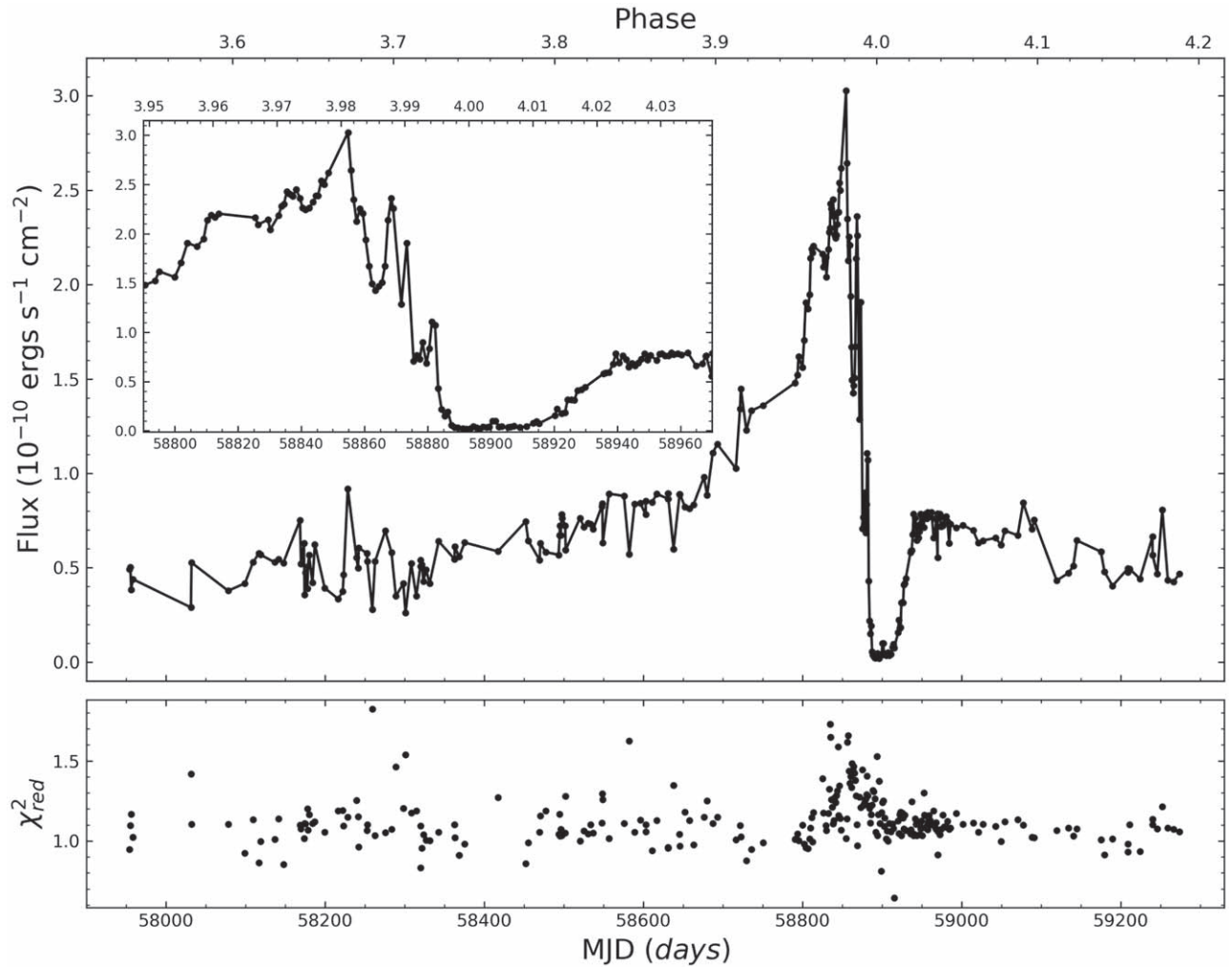


**Figure 7.** Flux between 2.0 and 10.0 keV observed by NICER. Fluxes are measured in the XSPEC command `FLUX`, fitting a three collisional ionized plasma model with a Gaussian for the Fe–K line. The bottom panel shows the reduced  $\chi^2$  from the fittings. At this point in our analysis, the background subtraction becomes more important, since the goodness of the fit is highly affected if the background is not properly subtracted. Both background estimators improve the goodness of the fit, but the 3C50 estimator shows more stable behavior over the whole data set of observations.

below 2 keV. As the flux increases, the column density measures become more precise and show a quasi-exponential increase, reaching a maximum value of  $N_H \approx 10^{24}$   $cm^{-2}$  at the end of the deep X-ray minimum. Note that near the X-ray minimum, determining the column density precisely is difficult, because the flux level is so low and the spectrum is not well defined in the individual NICER observations. After reaching the maximum, the measured column densities show a quasi-exponential decline through the shallow minimum, which appears to be fairly symmetric to the quasi-exponential increase seen through the deep minimum. This is somewhat surprising, since the distortion of  $\eta$ Car-A’s wind is very different before the X-ray minimum and afterward, as shown by hydrodynamical modeling (see, for example, Madura et al. 2013).

Figure 11 also shows previous column density measures from the literature and the column densities determined from a new analysis of the available CHANDRA High Energy Transmission Grating spectra (D. Espinoza-Galeas et al. 2022, in preparation). In general, there is good agreement between the NICER column densities and the Swift column densities obtained during the previous periastron passage in 2014. There are significant discrepancies between the NICER column densities and the others measured from the “snapshot”

spectra obtained by Suzaku, XMM-Newton, and CHANDRA at some phases. In particular, the maximum column measured by Hamaguchi et al. (2014) is near  $10^{25}$   $cm^{-2}$ , about an order of magnitude larger than the maximum NICER column. It may be that the maximum NICER column has been underestimated, due to residual soft circumstellar emission in the NICER field of view and due to the uncertainties on the background estimation. There are also large differences, up to an order of magnitude, during the high-absorption interval following the X-ray minimum, between the Hamaguchi et al. (2007b) measures, the CHANDRA measures, and the Swift and NICER column densities. The column densities and temperatures that we derive from our analysis of the NICER spectra differ from those derived by Kashi et al. (2021). These differences are mostly due to the different methods used in the spectral analysis. Kashi et al. (2021), following Hamaguchi et al. (2007b), apparently derived their column densities and temperatures by fitting the hard-band portion of the spectrum with a simple absorbed one-temperature model (see their Table 2). Their analysis tends to underestimate the X-ray temperature, but overestimate the emission measure and column densities. We use a more realistic model, which describes the complex emission seen in the high-resolution

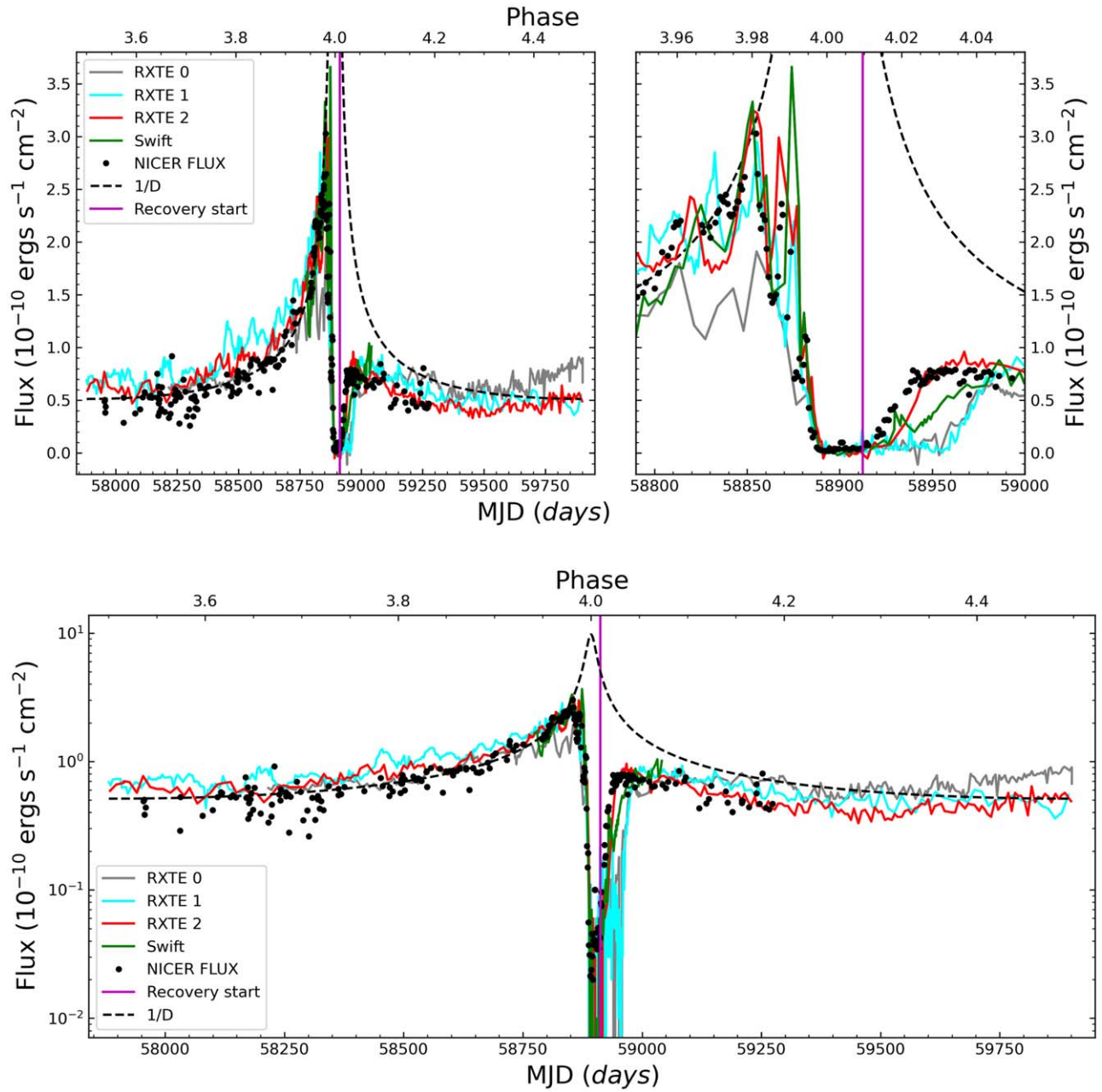


**Figure 8.** Top: comparison of the 2–10 keV band fluxes from NICER and earlier RXTE and Swift observations from Corcoran et al. (2017). The earlier measures have been advanced by 4, 3, 2, and 1 periods for RXTE cycles 0, 1, and 2 and the Swift data, respectively, for comparison to the NICER measures. A  $1/D$  curve is shown by the dashed line. Bottom: flux in log scale, to emphasize the depth of the X-ray minimum and the maximum height of the  $1/D$  curve.

CHANDRA spectra (as discussed above), and which also includes analysis of the lower-energy emission, which is most sensitive to column density changes. These temperatures are also consistent with the observed Fe XXVI/Fe xxv ratio  $\sim 0.1$ – $0.3$ , as seen in the CHANDRA spectra near the apastron (Espinoza-Galeas 2021).

#### 4.6. X-Ray Temperatures

The maximum X-ray temperature of the shocked gas in a colliding wind binary should be approximately constant with the orbital phase, if the preshock velocities of the winds are near terminal velocity at every point in the orbit. Figure 12 shows the temperatures for the higher-temperature component in our assumed two-temperature spectral model for the CWR

X-ray emission. The temperature of this higher-temperature component shows significant scatter for most of the orbit, as can be seen in the upper panel, but overall there is not much evidence for significant changes in temperature when the stars are well separated. In the interval  $3.5 < \phi < 3.9$ , the weighted average temperature for this component  $kT = 3.84 \pm 1.05$  keV. For comparison, Hamaguchi et al. (2007b) derived a temperature of  $kT = 4.6^{+0.2}_{-0.1}$  keV near  $\phi = 1.47$ . Over the entire orbit, the weighted average temperature is similar,  $kT = 3.74 \pm 1.06$  keV.

The bottom panel in Figure 12 shows the temperature variation near the X-ray maximum/minimum, in the phase range  $3.85 < \phi < 4.05$ . Temperature measures are more precise near the X-ray maximum, when the hard emission component

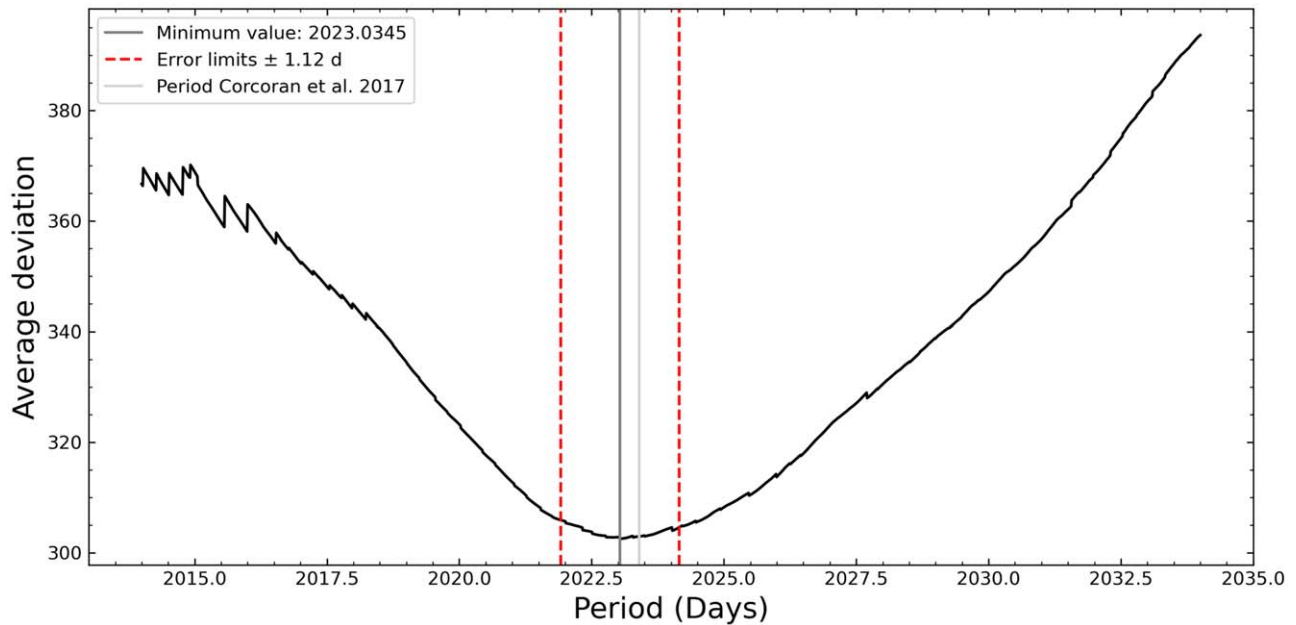


**Figure 9.** Sum of the square of the residuals for the RXTE, Swift, and NICER X-ray flux curves, phased for periods in the range of 2015–2035 days. Including the NICER data, the best X-ray period is 2023.035 days (dark gray line). The light gray line is the period calculated in Corcoran et al. (2017). The red lines are the limits of the error calculated in this work.

is bright. The temperatures at the X-ray minimum are not shown, because it is not possible to get reliable measurements from the NICER spectra between 2.0–10.0 keV, since the source is too faint. Starting from  $\phi > 4.10$ , the temperature is nearly constant at  $kT = 3.6 \pm 0.8$  keV, and it again shows more scatter starting from  $\phi = 4.06$ , with an average temperature near 4.0 keV. As can be seen from Figure 12, there is a significant, apparently monotonic, decline in the temperature of this component, starting at  $\phi = 3.96$ . This decline in temperature occurs before the plunge of  $\eta$  Car’s X-ray emission to the minimum, when the stars are moving toward each other, as they approach the point of periastron. The temperature shows a mostly linear decline from about  $4.5 \pm 0.4$  keV ( $T = 52.2 \times 10^6$  K) to approximately  $3.0 \pm 0.5$  keV ( $T = 34.8 \times 10^6$  K), over only 60 days, cooling at a rate of about  $3 \times 10^5$  K day $^{-1}$ . However, Hamaguchi et al. (2007b) measured higher temperatures in the phase range  $1.988 < \phi < 1.99$  from two XMM-Newton spectra obtained just before the 2003 X-ray minimum, reporting temperatures of  $kT = 4.5$  keV at 1.988 and 5.4 keV at 1.99, neither of which were consistent with the cooling during this interval in 2003. As a check on the phase-dependence of the hot-component temperature, we also measured the temperatures from the CHANDRA HETGS spectra obtained contemporaneously with the NICER observations, using the same spectral model (Espinoza-Galeas 2021). We found good agreement between the temperatures derived from the fits to the CHANDRA HETGS spectra and the NICER spectra, and, in particular, that the CHANDRA temperatures showed a similar monotonic decline in the phase interval 3.98–3.99.

We also measured the temperature of the cooler component. The cooler emission originates from gas farther downstream from the shock apex, and is a combination of hotter gas that has cooled as it has flowed away from the shock apex and lower-temperature shocked gas that is produced where the wind flows collide indirectly. The cool-component temperatures are often difficult to constrain because of the soft emission from the constant outer debris X-ray emission below 2 keV. Several of

the fits reach our assumed 1 keV lower constraint. The temperatures for this cooler component are easier to constrain near the X-ray maximum, when the source is bright, but also depend on an accurate assessment of the increasing absorption column. In the flare region close to the X-ray maximum, the temperatures of the cool component show interesting behavior, as can be seen in Figure 13. At phases between 3.97 and 4.00, the cool-component temperatures are somewhat higher than those at earlier phases, and show a possible correlation with the flares, where the higher flux seems to correspond to the higher values of the cool-component temperature.

## 5. Discussion

### 5.1. Changes in Mass-loss Rates

The X-ray emission measure and column density provide arguably the most robust measure of the variation in mass loss from the winds of  $\eta$  Car-A and  $\eta$  Car-B. This is because the 2–10 keV thermal emission is dependent on the density of the shocked wind of  $\eta$  Car-B along the shock front, while the absorption of this emission depends on the density profile of the wind of  $\eta$  Car-A, as the X-ray emission travels from the shock front through the wind of  $\eta$  Car-A to the observer. The excellent agreement in the derived column densities between the NICER and Swift observations shows that there has been no significant change in the mass-loss rate from  $\eta$  Car-A in the 2014–2020 time interval. There is also, generally, good agreement between the NICER column densities and most of the column densities from the earlier cycles measured by Hamaguchi et al. (2007b) and Hamaguchi et al. (2014), which suggests, for the most part, a fairly constant density profile through the wind of  $\eta$  Car-A. As shown in Figure 11, however, there are some disagreements between the NICER and Swift column densities and the earlier measures, particularly in the interval  $0.02 < \phi < 0.05$ , in which the Swift and NICER column densities are significantly lower than the two measures reported in Hamaguchi et al. (2007b) in this phase range. This

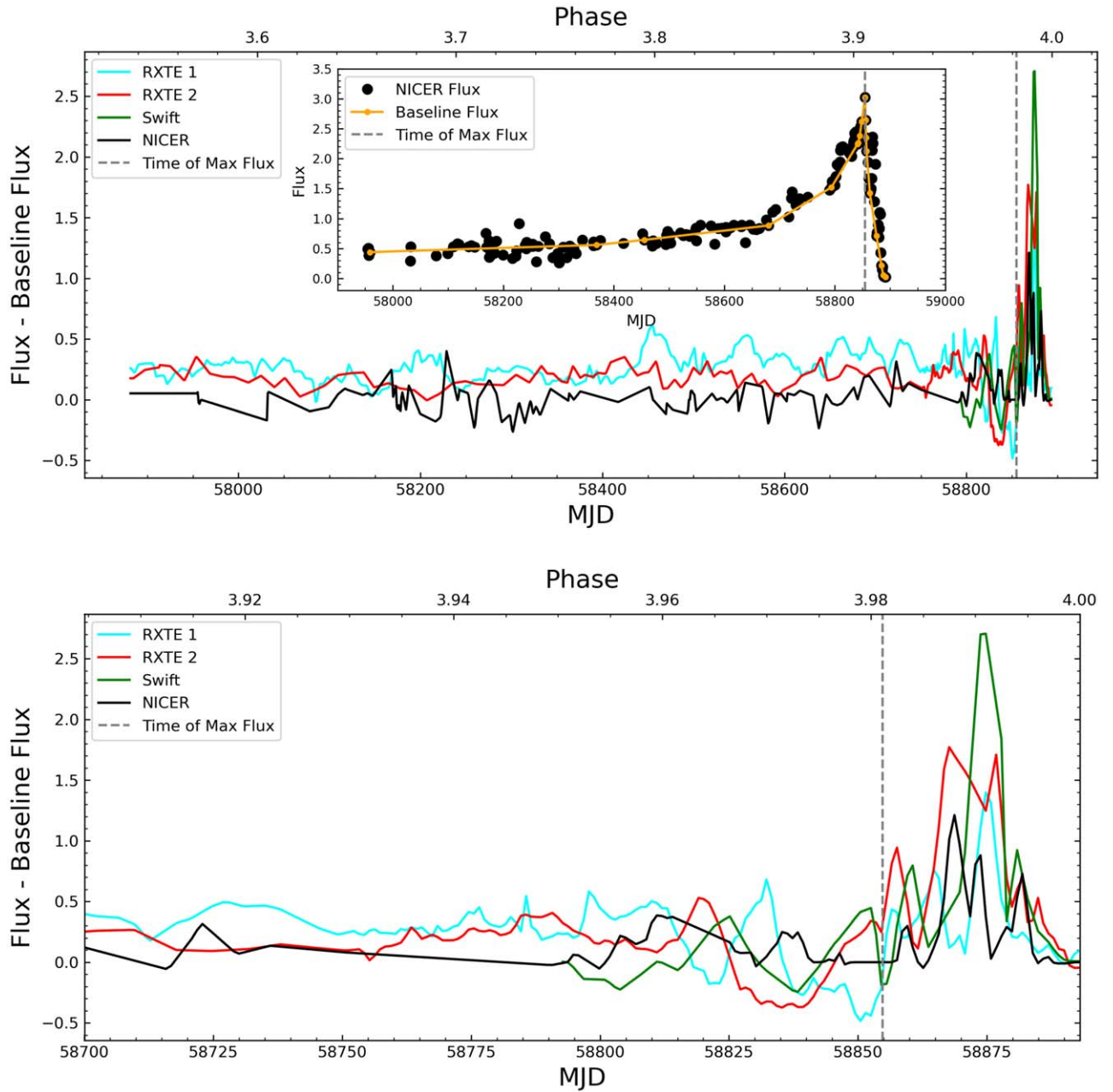


**Figure 10.** Top: residuals of NICER (black solid line), RXTE (cyan and red lines), and Swift (green line). The dashed vertical line shows the observed maximum of the X-ray count rate as seen by NICER. The inset shows the NICER X-ray 2–10 keV flux curve vs. MJD. The orange line shows the baseline flux used to calculate the residuals, which approximately follows a  $1/D$  variation before the maximum, then is followed by the lowest values during the plunge. Bottom: the same as the top, zooming in on the times close to the maximum X-ray emission and before the minimum X-ray emission.

discrepancy may indicate that a significant change in the wind density profile from  $\eta$  Car-A occurred sometime between 2003 and 2014. Conclusively deciding the nature of this discrepancy is difficult, because of the poor time sampling of the 2003 observations, and stochastic variations in the density profile caused by local clumping in the wind of  $\eta$  Car-A cannot be entirely ruled out (though the discrepancy, about a factor of 5 in the derived column densities at  $\phi \approx 0.04$ , seems large for a local perturbation that might be produced, for example, by a wind clump or other local density enhancement). At this phase, simulations show that the X-ray emission from the colliding wind bow shock passes through the distorted wind from  $\eta$  Car-A, as the wind is wrapped around the leading wall of the bow shock, and it is plausible that small stochastic changes in this

region of the wind could have large effects on the absorbing column.

Overall, the measured X-ray column densities from the 2003–2020 interval agree better than 40%–50% with the previous observations. Since the column density is directly proportional to  $\dot{M}$ , and since the NICER and Swift column densities tend to be lower than the earlier measurements, this agreement constrains the decline in the mass-loss rate from  $\eta$  Car-A,  $\dot{M}_A$ , to  $\dot{M}_A/\dot{M}_A < 2.5\%$  per year.

The X-ray flux in the 2–10 keV band depends on the emission measure of the shocked wind of  $\eta$  Car-B, which is proportional to the mass-loss rate from the companion,  $\dot{M}_B$ . Thus, comparing the fluxes in the 2–10 keV band from different orbital cycles provides a measure of the changes in

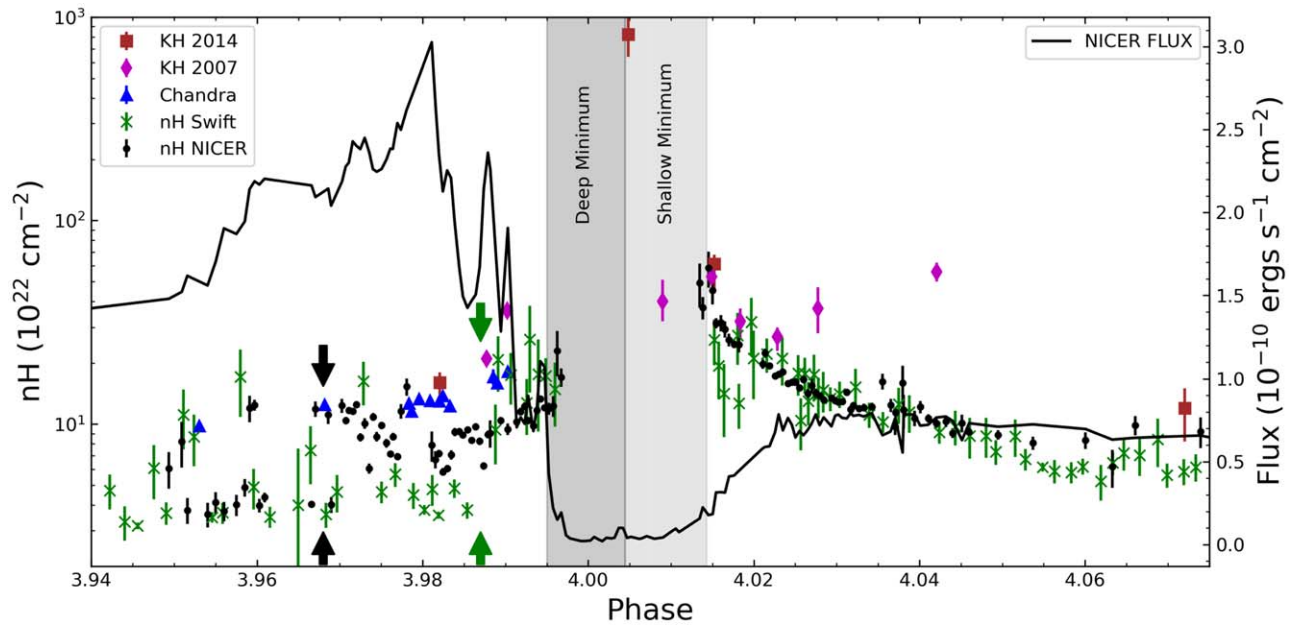


**Figure 11.** The column densities observed by NICER compared to the Swift column densities from the last orbital cycle (Corcoran et al. 2017). The magenta diamonds are the previous measurements from (Hamaguchi et al. 2007b), while the red squares are from the CHANDRA, XMM-Newton, and Suzaku spectra (Hamaguchi et al. 2014). The blue triangles are the column densities derived from analysis of the CHANDRA grating spectra (D. Espinoza-Galeas et al., 2022, in preparation). The gray regions mark the “deep” and “shallow” minima. Notice the good agreement in the Swift and NICER observations after the shallow minimum. The arrows mark the abrupt, steplike increase in column density (near  $\phi = 3.99$  for Swift and  $\phi = 3.97$  for NICER).

the mass-loss rate from the companion,  $\dot{M}_B$ , over time. It is best to compare the fluxes when the stars are close to the apastron, since the shock is stable and cooling is adiabatic. As shown in Figure 8, there is good agreement between the RXTE Cycle 1 (2003) and Cycle 2 (2009) observations near  $\phi \approx 3.8$ , while the RXTE Cycle 0 and NICER fluxes are about 25% lower. This could indicate nonmonotonic variability in the mass-loss rate from the companion; also, this could indicate some systematic error in the calibration between the RXTE Cycle 0 and NICER fluxes and the RXTE fluxes from the other two cycles. Kashi et al. (2021) suggest that  $\eta$  Car’s different X-ray emission recoveries are the result of a decrease in  $\eta$  Car-A’s wind. If this were the case, then we should expect significant differences in the column densities for different recoveries. But, as shown in Figure 11, the column densities in the recoveries observed by Swift and NICER are very similar, showing no significant changes in the mass-loss rate, despite the different recovery durations.

### 5.2. Shock Temperatures, Wind Velocities, and the Radius of $\eta$ Car-B

As seen in Figure 12, the hotter component shows a fairly constant X-ray temperature of  $kT = 3.84 \pm 1.05$  keV up to  $\phi \approx 3.96$ , after which there is a rather linear decline up to  $\phi = 3.99$  (at which point the spectra become too faint for analysis). The hottest plasma in the colliding wind shock originates near the apex of the shock cone, where the winds collide nearly head-on, and as the stars approach the periastron passage, the apex of the colliding wind shock moves closer to the companion star. If the apex enters the region of the companion’s wind where the wind is still accelerating and has not yet reached terminal velocity, this would cause a drop in the temperature of the hot shocked gas near the apex. The drop in temperature of  $\approx 2/3$  by  $\phi = 3.99$  compared to the temperature

at  $\phi = 3.96$ , when the decline apparently starts, suggests a drop in the preshock velocity of the fast wind of  $\eta$  Car-B. Since  $T \propto V^2$ , this corresponds to a decrease in the preshock velocity of the wind of  $\eta$  Car-B of  $(V_1 - V_2)/V_1 \approx 2.5\%$ , where  $V_1$  is the wind velocity at  $\phi = 3.96$  and  $V_2$  is the wind velocity at  $\phi = 3.99$ .

Figure 14 shows the expected variation in the separation of the two stars and the distance from  $\eta$  Car-B to the stagnation point of the shock, derived by balancing the pressure of the wind from  $\eta$  Car-A and  $\eta$  Car-B between the two stars. Figure 14 also shows the derived change in wind velocity, assuming a standard wind velocity law  $V(r) = V_{\infty,B}(1 - R_B/r)^\beta$ , where  $V(r)$  is the velocity of  $\eta$  Car-B’s wind at a distance  $r$  from the star,  $V_{\infty,B}$  is the terminal velocity of  $\eta$  Car-B’s wind, and  $\beta$  is the wind acceleration constant (usually close to 1 for most radiatively driven winds). Note that very near to the periastron, the apex moves very close to the companion and the velocity calculation breaks down. The dashed vertical gray lines indicate the phase interval of the observed cooling of the hotter component, while the red line shows the change in wind velocity implied by the temperature decreases, assuming  $T \propto V^2$ . The intersections of the dashed vertical gray line and the red line show the derived velocities at the start and end of the observed cooling interval, respectively. We find that the derived change in wind velocity is fairly well matched by the calculated variation in  $\eta$  Car-B’s preshock wind velocity at the distance of the shock cone apex over this range of orbital phase, if the radius of  $\eta$  Car-B is  $\approx 30 R_\odot$ . Ionization modeling by Verner et al. (2005) yielded values of  $T_{\text{eff},B} = 37,200$  K and  $\log L_B/L_\odot \approx 5.97$ , implying an effective radius of  $23.6 R_\odot$ , slightly smaller than the radius that reasonably describes the X-ray cooling if  $\beta = 1$ , as shown in Figure 14; but, given the uncertainties and assumptions, these numbers are in good agreement. On the other hand, the photoionization modeling by Mehner et al. (2010) suggests a somewhat hotter but fainter companion star,  $T_{\text{eff},B} = 39,000$  K and  $\log L_B/L_\odot \approx 5.60$ , yielding an effective radius of only



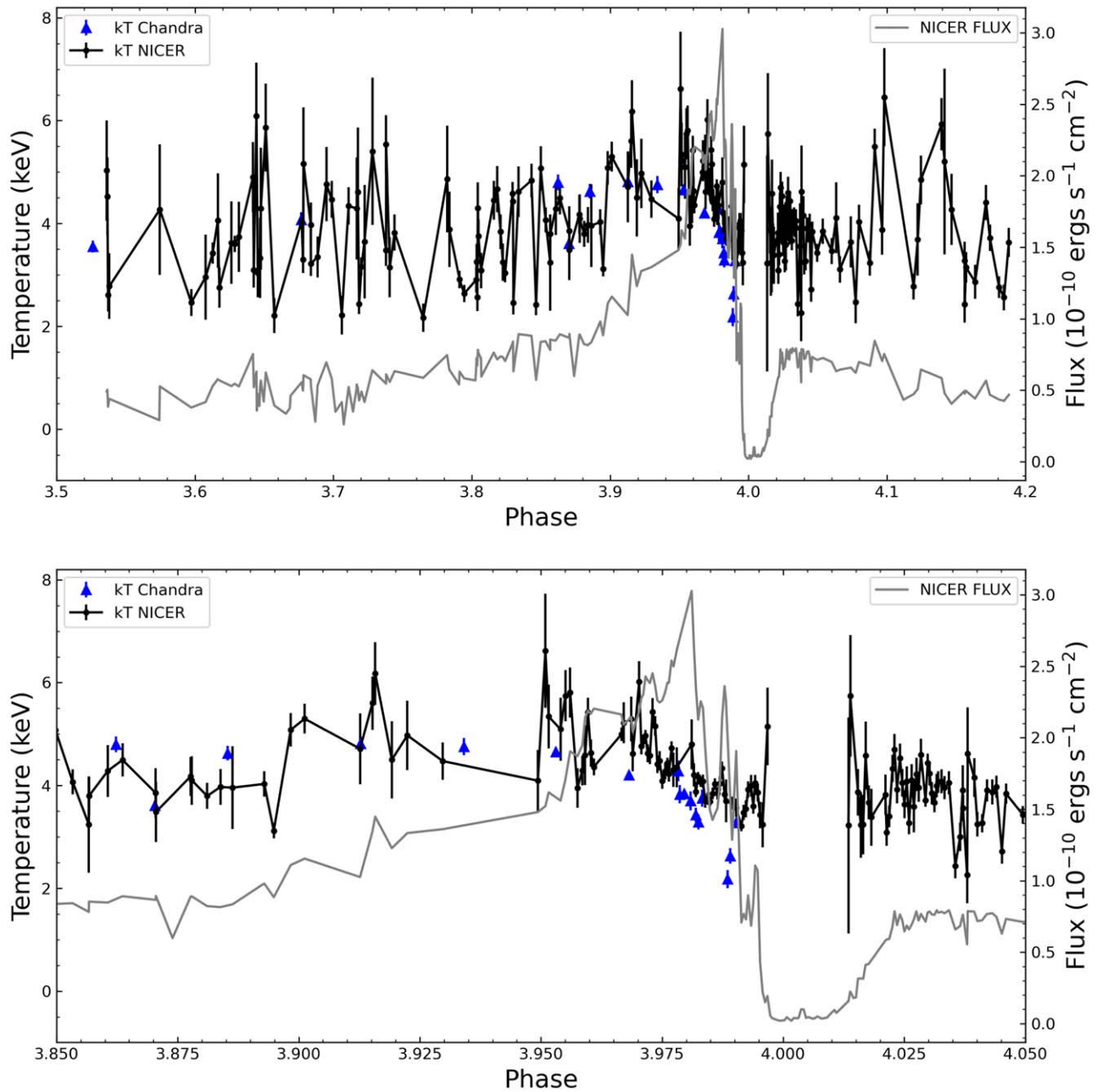


**Figure 12.** Top: temperature vs. phase of the hot component for the  $\eta$  Car NICER observations in this work. Bottom: the same as the top panel, near the X-ray minimum ( $3.85 < \phi < 4.05$ ). A clear decline in temperature can be seen, starting at  $\phi \approx 3.97$ , a phase when the 2–10 keV X-ray flux is still increasing. By  $\phi \approx 4.02$ , the temperature has stabilized around 4.0 keV, with increased variability after  $\phi \approx 4.06$ . Note that the spectrum is too faint during the X-ray minimum ( $3.995 < \phi < 4.015$ ) for a reliable measure of the X-ray temperatures.

$14.0 R_{\odot}$ . We can reasonably describe the observed X-ray cooling curve with these radii, but both require higher values of  $\beta$  (indicating a more slowly accelerating wind)— $\beta \approx 1.5$  and  $\beta \approx 3.0$  for the Verner et al. (2005) and Mehner et al. (2010) radii, respectively.

### 5.3. The Deep/Shallow Minimum Transition

The NICER campaign has provided the best measure obtained so far for the variations in X-ray flux and X-ray spectral properties around the X-ray minimum. The NICER HR in Figure 4 shows the transition between the “deep” and “shallow” states of the X-ray minimum, first identified by Hamaguchi et al. (2014) from a set of only five CHANDRA

ACIS spectra. Figure 4 also show that the deep minimum interval lasts for an interval of 18 days, starting at  $\phi = 3.995$  and ending at  $\phi = 4.004$ , with the transition to the shallow minimum. The shallow interval ends at  $\phi = 4.013$ , a duration of 18 days, while the shock gradually strengthens and the absorption dissipates as the companion moves around and away from  $\eta$  Car-A. This is consistent with the interpretation offered in Hamaguchi et al. (2014), who suggested that the deep minimum is produced by the occultation of the X-ray-emitting gas by the optically thick inner wind of  $\eta$  Car-A, which completely hides the X-ray emission from the colliding wind shock, plus a decline in the X-ray emissivity near the periastron passage, followed by a gradual strengthening of the shock and a reheating to X-ray-emitting temperatures.

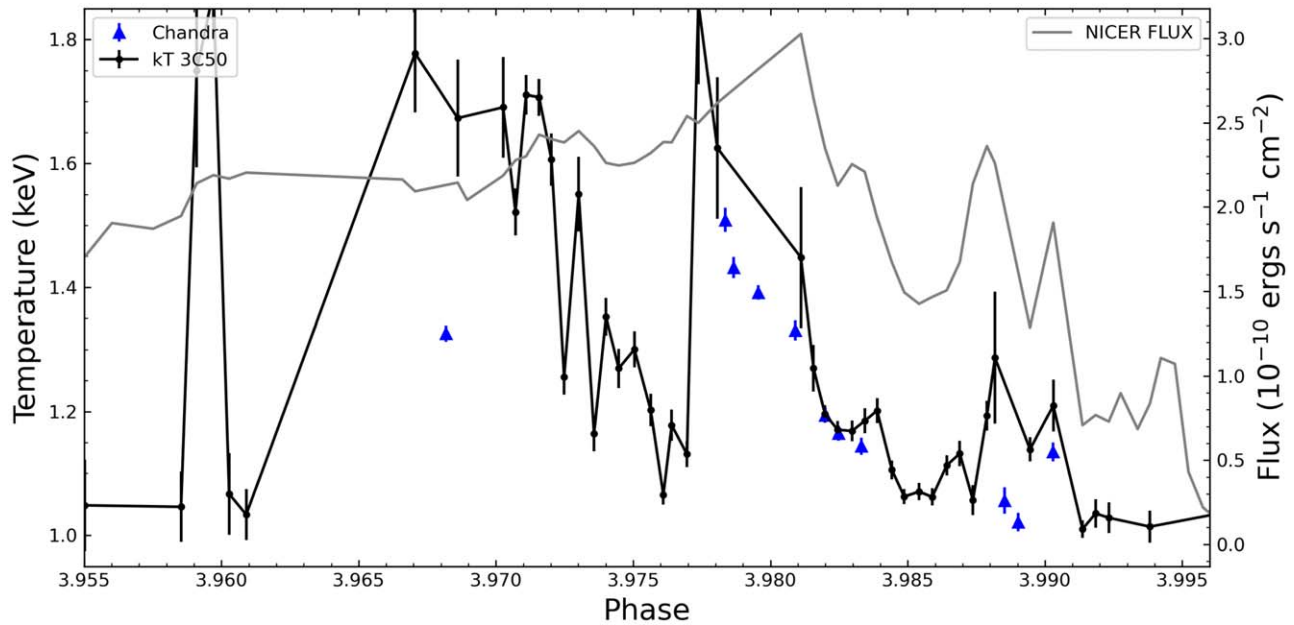


**Figure 13.** NICER temperatures vs. phase for the cool component between phases 3.95 and 4.00. The flare region shows an apparent correlation between temperature and flux, where the peak of the cool-component temperature appears to coincide with the flare peaks.

#### 5.4. The Column Density Variation through $\eta$ Car's Orbital Motion

The column density from the hot component of the  $\eta$  Car X-ray emission shows variability throughout the NICER monitoring program. Those changes go up to one order of magnitude in column density (Figure 11), with intervals no longer than  $\sim 0.1$  in phase. The variations indicate the changes in the amount of material in front of the apex of the CWR in our line of sight. The occurrence and duration of the  $N_H$  variations before  $\phi = 3.95$  do not show a particular correlation with flux or phase. Stochastic changes in  $\eta$  Car-A's wind by clumps could explain the variability observed. The lack of more frequent observations before  $\phi = 3.95$  makes a deeper analysis of those variations in column density difficult.

After  $\phi = 3.94$ , more frequent NICER observations were allocated. Between phases 3.96 and 3.97, the  $N_H$  shows a particular stability in the measurements. The stability of so many subsequent measurements had not been observed before. The measurements of  $N_H$  between  $3.97 < \phi < 3.98$  make clear the increase by one order of magnitude in column density after phase 3.98. After  $\phi = 3.98$ , the column density remains almost constant for the next  $\Delta\phi \approx 0.1$ . The step of one order of magnitude at  $\phi = 3.97$  could also be due a clump in the  $\eta$  Car-A wind. Another interesting explanation for the step change in column density is the transition between the wind from  $\eta$  Car-B and  $\eta$  Car-A, separated by the walls of the cone formed by the CWR.

#### 5.5. Variation in the Duration of the X-Ray Minimum

As first noted by Espinoza-Galeas et al. (2020), NICER showed that the duration of the X-ray minimum in 2020 was the shortest seen in any of the four orbital cycles monitored so far. The first two minima seen by RXTE, in 1997 and 2003, had nearly identical X-ray minimum durations, while the RXTE monitoring of the 2009 minimum had a significantly shorter duration. Any hypothesis needs to explain the apparently stochastic behavior observed in the starting time

of the X-ray recovery observed in Figure 8. Corcoran et al. (2010) suggested that the different recoveries were due to a decline in  $\eta$  Car's wind momentum. This decline could have been caused by a drop in mass loss or wind terminal velocity, or some combination of the two. If so, we might expect to see differences in column densities when comparing the X-ray spectra obtained during the recovery in different orbital cycles. Figure 11 compares the column densities from cycle 3 (Swift) and cycle 4 (NICER). Although the duration of the cycle 3 minimum was substantially longer than the cycle 4 recovery (see Figure 8), after  $\phi \approx 4.020$  the column densities from Swift and NICER are very similar. This suggests that the differences in the durations of the cycle 3 and cycle 4 minima were not produced by a significant change in the wind momentum of the primary. Kashi et al. (2021) and Kashi & Soker (2009) propose that accretion at the periastron weakens the mass-loss rate of  $\eta$  Car-A every cycle, implying that any new X-ray emission recovery should be shorter than the previous one. But, as discussed above, it is not likely that  $\eta$  Car-A's wind has weakened significantly from 2015 to 2020, based on the column densities. Also, the 2009 minimum was shorter than the 2015 minimum, as shown in Figure 8, indicating that there has been no systematic weakening of  $\eta$  Car-A's wind with time.

The comparison of the NICER and Swift observations around the X-ray minimum suggests that another mechanism is producing the variation in the durations of the X-ray recoveries. Winds from luminous hot stars are prone to line-deshadowing instabilities (LDIs) that can randomly create localized variations in wind density (Owocki et al. 1988). Figure 4 in Owocki et al. (1988) shows how those instabilities can increase the velocity of the wind from  $\sim 500$  to  $\sim 1250$  km s $^{-1}$ , especially in the dense inner parts of the wind. Such local density enhancements (clumps) interacting with the colliding wind bow shock can move the stagnation point of the CWR closer to  $\eta$  Car-B, reducing the preshock wind speed and reducing the hot X-ray flux from the bow shock. In this scenario, we can still have regions where the shock of the wind can generate high-energy X-rays, but these are distributed over a broader region,

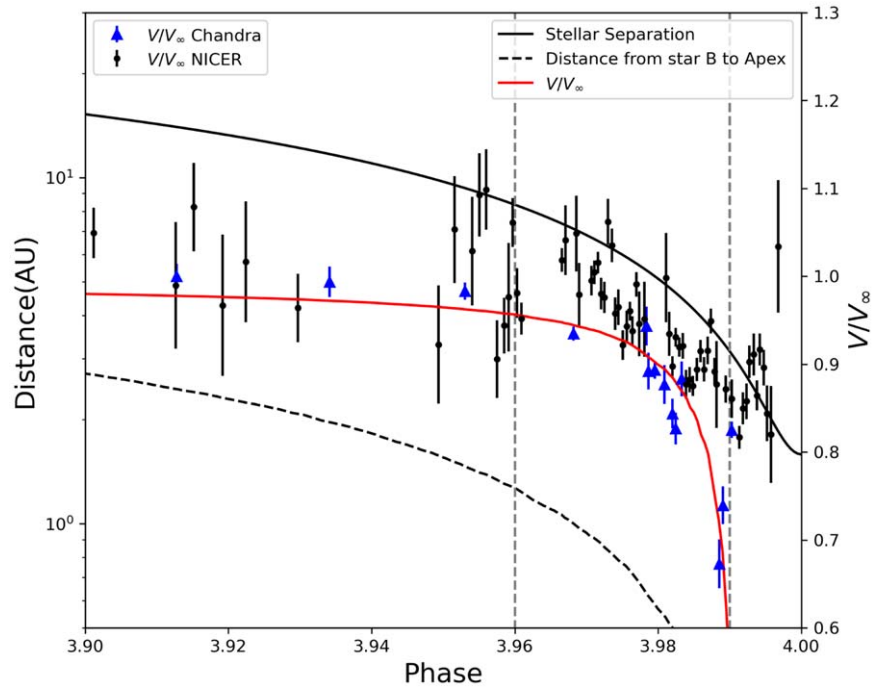


**Figure 14.** The Figure shows the expected variation in stellar separation (solid black line) with the  $v/v_\infty$  of  $\eta$  Car-B’s wind at the location of the apex (red line), derived using the system and stellar parameters given in Table 1, and a radius of  $\eta$  Car-B =  $30 R_\odot$ . The gray vertical dashed lines indicate the observed phase interval of the decline in the X-ray temperature of the hot component.

which, together with the high column density, produce the shallow minimum. The shallow minimum duration will be dependent on the size of the clump and the time when the clump forms. Once the clump passes the shock,  $\eta$  Car-B’s wind can accelerate enough to reform the hot shocked gas in the CWR between the stars, starting the recovery of the hard X-ray flux.

We suggest that the sudden steplike increase in column density before the X-ray minimum (see Figure 11) indicates the formation of a dense clump produced by LDIs in the inner wind of  $\eta$  Car-A. This step is observed at a later phase in cycle 3 than in cycle 4, suggesting a connection between the clump formation time and the time of the recovery. Clumps that form later produce a longer X-ray minimum, while clumps that form earlier in the orbital phase pass beyond the bow shock earlier, producing an earlier X-ray recovery and a shorter X-ray minimum.

### 5.6. The Nature of Rapid X-Ray Variability

As discussed in Section 4.4, NICER observed similar rapid X-ray variability, or “flares,” which become evident near the X-ray maximum and are even seen during the decline to the minimum. The comparison of the NICER 2–10 keV X-ray fluxes with those from RXTE Cycle 1 and Cycle 2 as a function of time shows no strong correlation. Moffat & Corcoran (2009) concluded that this flaring activity was produced by large, homologously expanding localized overdensity regions, or clumps, in the wind of  $\eta$  Car-A.

The apparent coincidence of the peaks in the temperature of the cool component with the peaks of some X-ray flares, as seen in Figure 13, can be interpreted in terms of the “clump” model of Moffat & Corcoran (2009). In this model, the pressure of a clump on the wall of the bow shock downstream from the apex could, in principle, decrease the opening angle of

the bow shock, causing the winds to collide more directly, thereby increasing the temperature of the downstream shocked wind, while also increasing the density of that portion of the shock producing an increase in X-ray flux from the shocked wind of the companion star.

## 6. Conclusions and Future Work

NICER provides time-resolved measures of the 0.4–10 keV  $\eta$  Car X-ray spectrum from  $\phi \sim 3.5$  onward. The flux measured by NICER follows the  $1/D$  behavior for most of the orbit, similar to the RXTE and Swift lightcurves. NICER observed that the plunge of the X-ray maximum started at  $\phi \sim 3.98$ , similar to previous cycles, indicating that it is strongly correlated with orbital phase. An inspection of  $\eta$  Car’s NICER spectrum does not show evidence of a decrease in X-rays due to absorption, suggesting that the decrease in flux is due to a decrease in the temperatures at the CWR. This is the first time we have evidence of temperature decreases in the CWR of  $\eta$  Car. The temperature of the hot component declines on the approach to the periastron passage, indicating that the shock apex is moving into the acceleration zone of the wind of  $\eta$  Car-B.

The measurements of the HRs with NICER constrain the deep minimum to  $3.995 < \phi < 4.004$  (18 days) and the shallow minimum to  $4.004 < \phi < 4.013$ . We have observed the shortest X-ray recovery: the flux starts to increase at  $\phi = 4.009$ , which is  $\sim 7$  days earlier than the low limit estimated by Corcoran et al. (2010) in the 2009 periastron passage. The apastron fluxes do not change  $>5\%$ , indicating a change of no more than  $0.25\%$  in  $\dot{M}$  from  $\eta$  Car-A or  $\eta$  Car-B. The absorption measured by NICER shows an agreement up to 90% after  $\phi = 4.01$ , giving us another indicator that the  $\dot{M}$  from  $\eta$  Car-A or  $\eta$  Car-B has not changed significantly over the last two cycles.

The changes in the soft-band emission from the OE seen for the first time by NICER may be caused by the expansion of the ejecta. If so, simple analysis indicates that the X-ray luminosity near the time of the Great Eruption was about  $\sim 10^{41}$  ergs  $s^{-1}$ . This is the first estimate of the X-ray luminosity of the Great Eruption and suggests that the X-ray luminosity at that time was comparable to the total luminosity at longer wavelengths.

D.E.G. gratefully acknowledges support from NASA grants #80NSSC19K1451 and #80NSSC21K0092, and SAO grant #GO9-20015A, through NASA. This work was conducted as part of doctoral research conducted at The Catholic University of America. M.F.C. and K.H. are supported under the CRESST-II cooperative agreement #80GSFC17M0002 with the NASA/Goddard Space Flight Center. C.M.P.R. was supported by SAO grant #GO0-21006A through NASA; this

support is gratefully acknowledged. This research has made use of data and software provided by the High Energy Astrophysics Science Archive Research Center (HEASARC), which is a service of the Astrophysics Science Division at NASA/GSFC. This research has made use of NASA's Astrophysics Data System. This research has made use of Astropy,<sup>21</sup> a community-developed core Python package for Astronomy (Astropy Collaboration et al. 2013, 2018).

*Software:* XSPEC (Arnaud 1996), astropy (The Astropy Collaboration 2013, 2018).

## Appendix

Tables 6 and 7 include logs of the NICER observations and the NICER spectral modeling parameters, respectively.

**Table 6**  
Log of NICER Observations and Rates

OBSID	MJD Start	MJD End	Phase	EXPOSURE s	2.0–10.0 keV		2.0–3.0 keV		5.0–7.0 keV	
					Total cts/s	Net	Total cts/s	Net	Total cts/s	Net
1110010101	57954.1245	57954.9641	3.5343	299.7	6.09	$5.55 \pm 0.14$	2.66	$2.54 \pm 0.09$	0.71	$0.60 \pm 0.05$
1110010102	57955.0252	57955.9950	3.5347	677.0	6.69	$5.83 \pm 0.10$	2.83	$2.67 \pm 0.06$	0.83	$0.64 \pm 0.04$
1110010103	57956.1829	57956.8311	3.5352	636.5	6.59	$4.94 \pm 0.10$	2.82	$2.54 \pm 0.07$	0.82	$0.44 \pm 0.04$
1110010105	57958.4340	57958.6970	3.5362	392.9	6.51	$5.39 \pm 0.13$	2.70	$2.48 \pm 0.08$	0.81	$0.55 \pm 0.05$
1110010106	58031.0912	58031.8693	3.5723	297.1	7.07	$3.47 \pm 0.15$	3.15	$2.63 \pm 0.10$	0.85	<0.05
1110010107	58032.2539	58032.2613	3.5727	199.5	9.73	$6.33 \pm 0.22$	3.45	$2.93 \pm 0.13$	1.44	$0.62 \pm 0.09$
1110010108	58078.2795	58078.3071	3.5954	694.8	6.79	$4.92 \pm 0.10$	2.87	$2.56 \pm 0.06$	0.85	$0.42 \pm 0.04$
1110010109	58099.2565	58099.3248	3.6058	163.3	6.74	$5.40 \pm 0.20$	2.99	$2.73 \pm 0.14$	0.80	$0.49 \pm 0.07$

(This table is available in its entirety in machine-readable form.)











**Table 7**  
NICER Spectral Modeling Parameters

OBSID	Phase	Flux $10^{-11}$ ergs $cm^{-2}$ $s^{-1}$	NH <sub>3</sub> $10^{22}$ $cm^{-2}$	kT <sub>4</sub> keV	EM <sub>4</sub> $10^{58}$ $cm^{-3}$	NH <sub>5</sub> $10^{22}$ $cm^{-2}$	kT <sub>6</sub> keV	EM <sub>6</sub> $10^{58}$ $cm^{-3}$	Flux <sub>FeK</sub> $10^{-5}$ photons $cm^{-2}$ $s^{-1}$
1110010101	3.53	4.96	$3.24 \pm 0.25$	$1.01 \pm 0.11$	$0.74 \pm 0.18$	$3.43 \pm 0.89$	$5.91 \pm 1.18$	$0.30 \pm 0.04$	$6.46 \pm 4.40$
1110010102	3.53	5.03	$3.25 \pm 0.14$	$1.32 \pm 0.09$	$0.97 \pm 0.10$	$10.77 \pm 2.45$	$4.40 \pm 0.83$	$0.40 \pm 0.08$	$5.83 \pm 3.08$
1110010103	3.54	3.84	$3.37 \pm 0.44$	<1	$0.50 \pm 0.18$	$3.43 \pm 0.46$	$2.64 \pm 0.42$	$0.50 \pm 0.14$	$1.58 \pm 2.87$
1110010105	3.54	4.35	$3.59 \pm 0.17$	$1.14 \pm 0.09$	$1.21 \pm 0.15$	$14.52 \pm 4.55$	$2.43 \pm 0.71$	$0.89 \pm 0.53$	$6.38 \pm 3.94$
1110010106	3.57	2.65	$3.73 \pm 0.37$	$1.29 \pm 0.15$	$1.31 \pm 0.43$				
1110010107	3.57	5.15	$3.00 \pm 1.37$	$1.00 \pm 0.46$	$0.29 \pm 0.19$	$3.00 \pm 1.24$	$3.52 \pm 0.90$	$0.49 \pm 0.13$	$9.54 \pm 8.21$
1110010108	3.60	3.57	$3.00 \pm 4.25$	$1.30 \pm 0.59$	$0.12 \pm 0.12$	$3.00 \pm 0.71$	$2.13 \pm 0.15$	$0.66 \pm 0.10$	$2.09 \pm 2.98$
1110010109	3.61	3.93	$3.00 \pm 2.36$	$1.51 \pm 0.39$	$0.90 \pm 0.60$	$3.44 \pm 1.23$	$2.47 \pm 0.51$	$0.54 \pm 0.18$	$4.98 \pm 5.77$

(This table is available in its entirety in machine-readable form.)

<sup>21</sup> <http://www.astropy.org>

## ORCID iDs

David Espinoza-Galeas  <https://orcid.org/0000-0003-2971-0439>  
 M. F. Corcoran  <https://orcid.org/0000-0002-7762-3172>  
 K. Hamaguchi  <https://orcid.org/0000-0001-7515-2779>  
 T. R. Gull  <https://orcid.org/0000-0002-6851-5380>  
 N. D. Richardson  <https://orcid.org/0000-0002-2806-9339>  
 G. Weigelt  <https://orcid.org/0000-0001-9754-2233>  
 Augusto Damineli  <https://orcid.org/0000-0002-7978-2994>  
 Ian R. Stevens  <https://orcid.org/0000-0001-7673-4340>  
 K. Gendreau  <https://orcid.org/0000-0001-7115-2819>  
 Felipe Navarete  <https://orcid.org/0000-0002-0284-0578>

## References

- Anders, E., & Grevesse, N. 1989, *GeCoA*, **53**, 197
- Arnaud, K. A. 1996, in ASP Conf. Ser., 101, *Astronomical Data Analysis Software and Systems V*, ed. G. H. Jacoby & J. Barnes (San Francisco, CA: ASP), 17
- Arzoumanian, Z., Gendreau, K. C., Baker, C. L., et al. 2014, *Proc. SPIE*, **9144**, 914420
- Astropy Collaboration, Price-Whelan, A. M., Sipőcz, B. M., et al. 2018, *AJ*, **156**, 123
- Astropy Collaboration, Robitaille, T. P., Tollerud, E. J., et al. 2013, *A&A*, **558**, A33
- Corcoran, M. F. 2005, *AJ*, **129**, 2018
- Corcoran, M. F., Hamaguchi, K., Gendreau, K., et al. 2019, *ATel*, **13327**, 1
- Corcoran, M. F., Hamaguchi, K., Pittard, J. M., et al. 2010, *ApJ*, **725**, 1528
- Corcoran, M. F., & Ishibashi, K. 2012, in *Eta Carinae and the Supernova Impostors*, ed. K. Davidson & R. M. Humphreys, Vol. 384 (Boston, MA: Springer), 195
- Corcoran, M. F., Ishibashi, K., Swank, J. H., & Petre, R. 2001, *ApJ*, **547**, 1034
- Corcoran, M. F., Rawley, G. L., Swank, J. H., & Petre, R. 1995, *ApJL*, **445**, L121
- Corcoran, M. F., Petre, R., Swank, J. H., et al. 1998, *ApJ*, **494**, 381
- Corcoran, M. F., Liburd, J., Morris, D., et al. 2017, *ApJ*, **838**, 45
- Corcoran, M. F., Hamaguchi, K., Espinoza, D., et al. 2020, *ATel*, **13516**, 1
- Damineli, A. 1996, *ApJL*, **460**, L49
- Damineli, A., Conti, P. S., & Lopes, D. F. 1997, *NewA*, **2**, 107
- Damineli, A., Hillier, D. J., Corcoran, M. F., et al. 2008, *MNRAS*, **384**, 1649
- Davidson, K. 1971, *MNRAS*, **154**, 415
- Davidson, K., & Humphreys, R. M. 1997, *ARA&A*, **35**, 1
- Espinoza-Galeas, D. A. 2021, PhD thesis, The Catholic Univ. America
- Espinoza-Galeas, D. A., & Corcoran, M. F. 2020, AAS Meeting, **235**, 377.04
- Espinoza-Galeas, D. A., Corcoran, M. F., Hamaguchi, K., et al. 2020, *ATel*, **13636**, 1
- Gaviola, E. 1950, *ApJ*, **111**, 408
- Gaviola, E. 1953, *ApJ*, **118**, 234
- Gendreau, K. C., Arzoumanian, Z., & Okajima, T. 2012, *Proc. SPIE*, **8443**, 844313
- Groh, J. H., Hillier, D. J., Madura, T. I., & Weigelt, G. 2012, *MNRAS*, **423**, 1623
- Hamaguchi, K., Corcoran, M. F., Gull, T., et al. 2007a, in ASP Conf. Ser. 367, *Massive Stars in Interactive Binaries*, ed. N. Louis, St. & A. F. J. Moffat (San Francisco, CA: ASP), 257
- Hamaguchi, K., Corcoran, M. F., Gull, T., et al. 2007b, *ApJ*, **663**, 522
- Hamaguchi, K., Corcoran, M. F., Russell, C. M. P., et al. 2014, *ApJ*, **784**, 125
- Hillier, D. J., Davidson, K., Ishibashi, K., & Gull, T. 2001, *ApJ*, **553**, 837
- Humphreys, R. M., & Martin, J. C. 2012, in *Eta Carinae and the Supernova Impostors*, ed. K. Davidson & R. M. Humphreys, Vol. 384 (Boston, MA: Springer), 1
- Immler, S., & Kuntz, K. D. 2005, *ApJL*, **632**, L99
- Ishibashi, K., Corcoran, M. F., Davidson, K., et al. 1999, *ApJ*, **524**, 983
- Kashi, A., Principe, D. A., Soker, N., & Kastner, J. H. 2021, *ApJ*, **914**, 47
- Kashi, A., & Soker, N. 2009, *ApJL*, **701**, L59
- Kiminki, M. M., Reiter, M., & Smith, N. 2016, *MNRAS*, **463**, 845
- Madura, T. I., Gull, T. R., Okazaki, A. T., et al. 2013, *MNRAS*, **436**, 3820
- Madura, T. I., Gull, T. R., Owocki, S. P., et al. 2012, *MNRAS*, **420**, 2064
- Mehner, A., Davidson, K., Ferland, G. J., & Humphreys, R. M. 2010, *ApJ*, **710**, 729
- Moffat, A. F. J., & Corcoran, M. F. 2009, *ApJ*, **707**, 693
- Morris, P. W., Gull, T. R., Hillier, D. J., et al. 2017, *ApJ*, **842**, 79
- Okazaki, A. T., Owocki, S. P., Russell, C. M. P., & Corcoran, M. F. 2008, *MNRAS*, **388**, L39
- Owocki, S. P., Castor, J. I., & Rybicki, G. B. 1988, *ApJ*, **335**, 914
- Parkin, E. R., Pittard, J. M., Corcoran, M. F., & Hamaguchi, K. 2011, *ApJ*, **726**, 105
- Parkin, E. R., Pittard, J. M., Corcoran, M. F., Hamaguchi, K., & Stevens, I. R. 2009, *MNRAS*, **394**, 1758
- Pittard, J. M., & Corcoran, M. F. 2002, *A&A*, **383**, 636
- Prigozhin, G., Gendreau, K., Doty, J. P., et al. 2016, *Proc. SPIE*, **9905**, 99051I
- Remillard, R. A., Loewenstein, M., Steiner, J. F., et al. 2021, *AJ*, **163**, 130
- Russell, C. M. P., Corcoran, M. F., Hamaguchi, K., et al. 2016, *MNRAS*, **458**, 2275
- Seward, F. D., Forman, W. R., Giacconi, R., et al. 1979, *ApJL*, **234**, L55
- Smith, N. 2006, *ApJ*, **644**, 1151
- Stellingwerf, R. F. 1978, *ApJ*, **224**, 953
- Stevens, I. R., Blondin, J. M., & Pollock, A. M. T. 1992, *ApJ*, **386**, 265
- Teodoro, M., Damineli, A., Heathcote, B., et al. 2016, *ApJ*, **819**, 131
- Usov, V. V. 1992, *ApJ*, **389**, 635
- Verner, E., Bruhweiler, F., & Gull, T. 2005, *ApJ*, **624**, 973
- Weis, K., Corcoran, M. F., Bomans, D. J., & Davidson, K. 2004, *A&A*, **415**, 595
- Wilms, J., Allen, A., & McCray, R. 2000, *ApJ*, **542**, 914